# Modeling of the chemistry in oxidation flow reactors with high initial NO

Zhe Peng and Jose L. Jimenez

Cooperative Institute for Research in Environmental Sciences and Department of Chemistry, University of Colorado, Boulder, CO 80309, USA
Correspondence to: J.L. Jimenez (jose.jimenez@colorado.edu)

**Abstract.** Oxidation flow reactors (OFRs) are increasingly employed in atmospheric chemistry research because of their high efficiency of OH radical production from low-pressure Hg lamp emissions at both 185 and 254 nm (OFR185) or 254 nm only (OFR254). OFRs have been thought to be limited to studying low-NO chemistry (where peroxy radicals ($RO_2$) react preferentially with $HO_2$) because NO is very rapidly oxidized by the high concentrations of $O_3$, $HO_2$, and OH in OFRs. However, many groups are performing experiments aging combustion exhaust with high NO levels, or adding NO in the hopes of simulating high-NO chemistry (where $RO_2$ + NO dominates). This work systematically explores the chemistry in OFRs with high initial NO. Using box modeling, we investigate the interconversion of N-containing species and the uncertainties due to kinetic parameters. Simple initial injection of NO in OFR185 can result in more $RO_2$ reacted with NO than with $HO_2$ and minor non-tropospheric photolysis, but only under a very narrow set of conditions (high water mixing ratio, low UV intensity, low external OH reactivity ($OHR_{ext}$), and initial NO concentration ($NO^{in}$) of tens to hundreds of ppb) that account for a very small fraction of the input parameter space. These conditions are generally far away from experimental conditions of published OFR studies with high initial NO. In particular, studies of aerosol formation from vehicle emissions in OFR often used $OHR_{ext}$ and $NO^{in}$ several orders of magnitude higher. Due to extremely high $OHR_{ext}$ and $NO^{in}$, some studies may have resulted in substantial non-tropospheric photolysis, strong delay to $RO_2$ chemistry due to peroxynitrate formation, VOC reactions with $NO_3$ dominating over those with OH, and faster reactions of OH-aromatic adducts with $NO_2$ than those with $O_2$, all of which are irrelevant to ambient VOC photooxidation chemistry. Some of the negative effects are worst for alkene and aromatic precursors. To avoid undesired chemistry, vehicle emissions generally need to be diluted by a factor of >100 before being injected into OFR. However, sufficiently diluted vehicle emissions generally do not lead to high-NO chemistry in OFR, but are rather dominated by the low-NO $RO_2$+$HO_2$ pathway. To ensure high-NO conditions without substantial atmospherically irrelevant chemistry in a more controlled fashion, new techniques are needed.

## 1 Introduction

The oxidation of gases that are emitted into the atmosphere, in particular volatile organic compounds (VOCs), is one of the most important atmospheric chemistry processes (Haagen-Smit, 1952; Chameides et al., 1988). VOC oxidation is closely related to radical production and consumption (Levy II, 1971), $O_3$ production, and formation of secondary aerosols (Odum et al., 1996; Hoffmann et al., 1997; Volkamer et al., 2006; Hallquist et al., 2009), which have impacts on air quality and climate (Lippmann, 1991; Nel, 2005; Stocker et al., 2014).

Chemical reactors are critical tools for research of VOC oxidation. Oxidation reactions of interest often have typical timescales of hours to weeks. Studying these processes in ambient air can be confounded by dispersion and changes in ambient conditions, which often occur on similar timescales. Chemical reactors allow for decoupling of these two types of processes. Also, they should be able to simulate the different regimes of reactions occurring in the atmosphere, e.g., VOC oxidation under low and high-NO conditions (peroxy radical fate dominated by reaction with $HO_2$ or with NO) representing remote and urban areas, respectively (Orlando and Tyndall, 2012).

Large environmental chambers are a commonly used reactor type (Carter et al., 2005; Wang et al., 2011). They typically employ actinic wavelength (>300 nm) light sources (e.g., outdoor solar radiation and UV blacklights) to produce oxidants and radicals and have large volumes (on the order of several cubic meters or larger). However, the capability of generating sustained elevated levels of OH, the most important tropospheric oxidant, is usually limited in chambers, resulting in OH concentrations similar to those in the atmosphere ($10^6$–$10^7$ molecules $cm^{-3}$; Mao et al., 2009; Ng et al., 2010), and consequently, long simulation times (typically hours) to reach OH equivalent ages of atmospheric relevance (George et al., 2007; Kang et al., 2007; Carlton et al., 2009; Seakins, 2010; Wang et al., 2011). The partitioning of gases and aerosols to chamber walls (usually made of Teflon) in timescales of tens of minutes to hours makes it difficult to conduct very long experiments that simulate high atmospherically-relevant photochemical ages (Cocker et al., 2001; Matsunaga and Ziemann, 2010; Zhang et al., 2014; Krechmer et al., 2016). In addition, the long simulation times and large size of chambers and auxiliary equipment are logistically difficult for field deployment, and their cost limits the number of laboratories equipped with them.

Given the limitations of environmental chambers, a growing number of experimenters have instead employed oxidation flow reactors (OFRs). OFRs have a much smaller size (of the order of 10 L), efficiently generate OH via photolysis of $H_2O$ and/or $O_3$ by more energetic 185 and 254 nm photons from low-pressure Hg lamps, and overcome the abovementioned shortcomings of chambers due to a much shorter residence time (George et al., 2007; Kang et al., 2007, 2011; Lambe et al., 2011). Moreover, OFRs are able to rapidly explore a wide range of OH equivalent ages within a short period (~2 hr), during which significant changes of ambient conditions can usually be avoided in the case of field deployment (Ortega et al., 2016; Palm et al., 2016, 2017). Because of these advantages, OFRs have recently been widely used to study atmospheric chemistry, in particular secondary organic aerosol (SOA) formation and aging, in both the laboratory and the field (Kang et al., 2011; Li et al., 2013; Ortega et al., 2013,

2016; Tkacik et al., 2014; Palm et al., 2016).

In addition to experimental studies using OFRs, there has also been some progress in the characterization of OFR chemistry by modeling. Li et al. (2015) and Peng et al. (2015) developed a box model for OFR $HO_x$ chemistry that predicts measurable quantities [e.g., OH exposure ($OH_{exp}$, in molecules $cm^{-3}$ s] and $O_3$ concentration (abbr. $O_3$ hereinafter, in ppm)] in good agreement with experiments. This model has been used to characterize $HO_x$ chemistry as a function of $H_2O$ mixing ratio (abbr. $H_2O$ hereinafter, unitless), UV light intensity (abbr. UV hereinafter, in photons $cm^{-2}$ $s^{-1}$), and external OH reactivity [in $s^{-1}$, $OHR_{ext}=\sum k_i c_i$, i.e., the sum of the products of concentrations of externally introduced OH-consuming species ($c_i$) and rate constants of their reactions with OH ($k_i$)]. Based on this characterization, Peng et al. (2015) found that OH suppression, i.e., reduction of OH concentration caused by $OHR_{ext}$, is a common feature under many typical OFR operation conditions. Peng et al. (2016) systematically examined the relative importance of non-OH/non-tropospheric reactants on the fate of VOCs over a wide range of conditions, and provided guidelines for OFR operation to avoid non-tropospheric VOC photolysis, i.e., VOC photolysis at 185 and 254 nm.

In previous OFR modeling studies, $NO_x$ chemistry was not investigated in detail, since in such in typical OFR experiments with large amounts of oxidants (e.g., OH, $HO_2$, and $O_3$), NO would be very rapidly oxidized and thus unable to compete with $HO_2$ for reaction with peroxy radicals ($RO_2$). Li et al. (2015) estimated an NO ($NO_2$) lifetime of ~0.5 (~1.5) s under a typical OFR condition. From these estimates, OFRs processing ambient air or laboratory air without large addition of $NO_x$ were assumed to be not suitable for studying oxidation mechanisms relevant to polluted conditions under higher NO concentrations. OFRs have recently been used to conduct laboratory experiments with very high initial $NO_x$ levels (Liu et al., 2015) and deployed to an urban tunnel, where $NO_x$ was high enough to be a major OH reactant (Tkacik et al., 2014). The former study reported evidence for the incorporation of nitrogen into SOA. Besides, OFRs have been increasingly employed to process emissions of vehicles, biomass burning, and other combustion sources (Table 1), where NO can often be hundreds of ppm (Ortega et al., 2013; Martinsson et al., 2015; Karjalainen et al., 2016; Link et al., 2016; Schill et al., 2016; Alanen et al., 2017; Simonen et al., 2017). It can be expected that such a high NO input together with very high VOC concentrations would cause a substantial deviation from good OFR operation conditions identified in Peng et al. (2016). Very recently, $N_2O$ injection has been proposed by Lambe et al. (2017) as a way to study oxidation of VOCs under high NO conditions in OFR. As more OFR studies at high $NO_x$ level are conducted, there is growing need to understand the chemistry of N-containing species in OFRs and whether it proceeds along atmospherically-relevant channels.

In this study, we present the first comprehensive model of OFR $NO_y$ chemistry. We extend the model of Li et al. (2015) and Peng et al. (2015) by including a scheme for $NO_y$ species. Then this model is used to investigate i) if an OFR with initial NO injection results in NO significantly reacting with $RO_2$ under any conditions, ii) if previously published OFR experiments with high initial NO concentrations led to $RO_2$+NO being dominant in VOC oxidation without negative side effects (e.g., non-tropospheric reactions), iii) how to avoid undesired chemistry in future studies. The results can provide insights into

the design and interpretation of future OH-oxidation OFR experiments with large amounts of $NO_x$ injection.

## 2 Methods

The physical design of the OFR modeled in the present work, the chemical kinetics box model, and the method of propagating and analyzing the parametric uncertainties on the model have already been introduced previously (Kang et al., 2007; Li et al., 2015; Peng et al., 2015). We only provide brief descriptions for them below.

### 2.1 Potential Aerosol Mass flow reactor

The OFR modeled in this study is the "Potential Aerosol Mass" (PAM) flow reactor, firstly introduced by Kang et al. (2007). The PAM OFR is a cylindrical vessel with a volume of ~13 L, equipped with low-pressure Hg lamps (model no. 82-9304-03, BHK Inc.) to generate 185 and 254 nm UV light. This popular design is being used by many atmospheric chemistry research groups, particularly those studying SOA (Lambe and Jimenez, 2017 and references therein). When the lamps are mounted inside Teflon sleeves, photons at both wavelengths are transmitted and contribute to OH production ("OFR185 mode"). In OFR185, $H_2O$ photolyzed at 185 nm produces OH and $HO_2$, while $O_2$ photolyzed at the same wavelengths results in $O_3$ formation. $O(^1D)$ is produced via $O_3$ photolysis at 254 nm and generates additional OH through its reaction with $H_2O$. 185 nm lamp emissions can be filtered by mounting the lamps inside quartz sleeves, leaving only 254 nm photons to produce OH ("OFR254 mode"). In this mode, injection of externally formed $O_3$ is necessary to ensure OH production. As the amount of $O_3$ injected is a key parameter under some conditions (Peng et al., 2015), we adopt the notation OFR254-X to denote OFR254 experiments with X ppm initial $O_3$ ($O_{3,in}$). In this study, we investigate OFR experiments with NO injected and thus utilize "OFR185-iNO" to describe the OFR185 mode of operation with initially (at the reactor entrance) injected NO. The same terminology is used for the OFR254 mode. For instance, the initial NO injection into OFR254-7 is denoted as OFR254-7-iNO.

### 2.2 Model description

The basic framework of the box model used in this study, a standard chemical kinetics model, is the same as in Peng et al. (2015). Plug flow is assumed in the model, since approximately taking residence time distribution into account leads to similar results under most conditions but at much higher computational expense (Peng et al., 2015). In addition to the reactions in the model of Peng et al. (2015), including all $HO_x$ reactions available in the JPL Chemical Kinetic Data Evaluation (Sander et al., 2011), all gas-phase $NO_y$ reactions available in the JPL database except those of organic nitrates and peroxynitrates are also considered in the current reaction scheme. An updated JPL evaluation was published recently (Burkholder et al., 2015), with slightly different (~20%) rate constants for $NO_2+HO_2+M \rightarrow HO_2NO_2+M$ and $NO_2+NO_3 \rightarrow N_2O_5$. The updated rate constants only result in changes of ~10–20% of the concentrations of the species directly consumed/produced by these reactions. These changes are smaller than the parametric uncertainties of the model (see Section 3.1.3). For other species, concentration changes are negligible. $HO_2NO_2+M \rightarrow HO_2+NO_2+M$ and $N_2O_5+M \rightarrow NO_2+NO_3+M$, are also included in the scheme, with kinetic parameters from the IUPAC Task Group on Atmospheric

Chemical Kinetic Data Evaluation (Ammann et al., 2016). As in Peng et al. (2015, 2016), $SO_2$ is used as a surrogate of external OH reactants (e.g., VOCs). $NO_y$ species, although also external OH reactants, are explicitly treated in the model and *not* counted in $OHR_{ext}$ in this work. Therefore, $OHR_{ext}$ stands for *non-*$NO_y$ $OHR_{ext}$ only hereinafter, unless otherwise stated. Also, particle-phase processes and interactions of gas-phase species with particles are not considered in this study. We have made this assumption because:

i) The presence of aerosols has typically negligible impacts on the gas-phase chemistry. Condensational sink (CS) of ambient aerosols can rarely exceed 1 $s^{-1}$ even in polluted areas and is usually 1-3 orders of magnitude lower (Donahue et al., 2016; Palm et al., 2016). Thus, even under the assumption of unity uptake coefficient, CS cannot compete with $OHR_{ext}$ (usually on the order of 10 $s^{-1}$) in OH loss. Uptake of NO onto aerosols only occurs through the reaction with $RO_2$ on particle surface (Richards-Henderson et al., 2015), which is formed very slowly (see below) compared to gas-phase $HO_x$ and $NO_x$ chemistry. Uptake of $HO_2$, $O_3$, $NO_3$ etc. is even more unlikely to be efficient (Moise and Rudich, 2002; Moise et al., 2002; Hearn and Smith, 2004; Lakey et al., 2015).

ii) On the other hand, gas-phase species have only limited impacts on OA. Heterogeneous oxidation of OA by OH is generally slow. Significant OA loss due to heterogeneous oxidation can only be seen at photochemical ages as high as weeks (Hu et al., 2016). The enhancement of heterogeneous oxidation due to NO is remarkable only at OH concentration close to the ambient values but not at typical values in OFR (Richards-Henderson et al., 2015).

It is an important approximation that the *real* $OHR_{ext}$ decay (due to not only primary VOC oxidation and subsequent oxidation, but also wall loss, partitioning to the particle phase, reactive uptake etc.) is surrogated by that of $SO_2$. Gas-phase measurements in literature laboratory studies revealed that there is a large variability of total $OHR_{ext}$ during (subsequent) oxidation of VOCs, depending on the type of precursors (Nehr et al., 2014; Schwantes et al., 2017). This variability is obviously mainly due to the evolution of different types of oxidation intermediates/products contributing to $OHR_{ext}$, but not due to changes in CS, wall conditions etc. Also this variability is difficult to accurately capture even if modeling with a mechanism as explicit as MCM is performed (Schwantes et al., 2017). It is thus justified to use a lumped surrogate to model the $OHR_{ext}$ decay for simplicity and efficiency. The uncertainties introduced by this approximation include those due to both the types of oxidation intermediates/products and all interactions of VOCs with aerosols, walls etc. And the uncertainties due to the former dominate over those due to the latter.

A residence time of 180 s and typical temperature (295 K) and atmospheric pressure (835 mbar) in Boulder, CO, USA are assumed for all model cases. The lower-than-sea level pressure only leads to minor differences in the outputs (Li et al., 2015). We explore physical input cases evenly spaced in a logarithmic scale over very wide ranges: $H_2O$ of 0.07%–2.3%, i.e., relative humidity (RH) of 2–71% at 295 K; 185 nm UV of $1.0\times10^{11}$–$1.0\times10^{14}$ and 254 nm UV of $4.2\times10^{13}$–$8.5\times10^{15}$ photons $cm^{-2}$ $s^{-1}$; $OHR_{ext}$ of

1–16000 $s^{-1}$; $O_{3,in}$ of 2.2–70 ppm for OFR254; initial NO mixing ratio ($NO^{in}$) from 10 ppt to 40 ppm. Besides, conditions with $OHR_{ext}$=0 are also explored. UV at 254 nm is estimated from that at 185 nm according to the relationship determined by Li et al. (2015). Several typical cases within this range as well as their corresponding 4 or 2-character labels (e.g., MM0V and HL) are defined in Table 2. Literature studies are modeled by adopting all reported parameters (e.g., residence time, $H_2O$, and $O_{3,in}$) and estimating any others that may be needed (e.g., UV) from the information provided in the papers.

In this study, OH equivalent ages are calculated under the assumption of an ambient OH concentration of $1.5x10^6$ molecules $cm^{-3}$ (Mao et al., 2009). Conditions leading to a ratio of $RO_2$ reacted with NO over the entire residence time [$r(RO_2+NO)$] to that with $HO_2$ [$r(RO_2+HO_2)$] larger than 1 are regarded as "high NO" (under the assumption of constant $OHR_{ext}$ from VOCs, see Section S1 for more details), where [r(X)] is the total reactive flux for reaction X over the entire residence time. $F185_{exp}/OH_{exp}$ and $F254_{exp}/OH_{exp}$ are used as measures of the relative importance of VOC photolysis at 185 and 254 nm to their reactions with OH, respectively [$F185_{exp}$ ($F254_{exp}$) are 185 (254) nm photon flux exposure, i.e., product of 185 (254) nm photon flux and time]. Readers may refer to Figs. 1 and 2 of Peng et al. (2016) for the determination of the relative importance of non-tropospheric (185 and 254 nm) photolysis of individual VOCs. Although the relative importance of non-tropospheric photolysis depends on individual VOCs, in the present work, we set criteria on $F185_{exp}/OH_{exp}<3x10^3$ cm/s and $F254_{exp}/OH_{exp}<4x10^5$ cm/s to define "good" conditions and $F185_{exp}/OH_{exp}<1x10^5$ cm/s and $F254_{exp}/OH_{exp}<1x10^7$ cm/s (excluding good conditions) to define "risky" conditions. Conditions with higher $F185_{exp}/OH_{exp}$ or $F254_{exp}/OH_{exp}$ are defined as "bad". Under good conditions, photolysis of most VOCs has a relative contribution <20% to their fate; under bad conditions, non-tropospheric photolysis is likely to be significant in all OFR experiments, since it can hardly be avoided for oxidation intermediates, even if the precursor(s) does not photolyze at all. Under risky conditions, some species photolyzing slowly and/or reacting with OH rapidly (e.g., alkanes, aldehydes, and most biogenics) still have a relative contribution of photolysis <20% to their fates, while species photolyzing more rapidly and/or reacting with OH more slowly (e.g., aromatics and other highly conjugated species and some saturated carbonyls) will undergo substantial non-tropospheric photolysis. Note that these definitions are slightly different than in Peng et al. (2016). All definitions of the types of conditions are summarized in Table 3.

### 2.3 Uncertainty analysis

We apply the same method as in Peng et al. (2014, 2015) to calculate and analyze the output uncertainties due to uncertain kinetic parameters in the model. Random samples following log-normal distributions are generated for all rate constants and photoabsorption cross sections in the model using uncertainty data available in the JPL database (Sander et al., 2011) or estimated based on IUPAC data (Ammann et al., 2016). Then, Monte Carlo Uncertainty Propagation (BIPM et al., 2008) is performed for these samples through the model to obtain the distributions of outputs. Finally, we compute squared correlation coefficients between corresponding input and output samples and apportion the relative contributions of individual kinetic parameters to the output uncertainties based on these coefficients

(Saltelli et al., 2005).

## 3 Results and discussion

In this section, we study the $NO_y$ chemistry in OFR while considering relevant experimental issues. Based on these results, we propose some guidelines for OFR operation for high-NO OH oxidation of VOCs.

### 3.1 $NO_y$ chemistry in typical OFR cases with initial NO injection

NO was thought to be unimportant (i.e., unable to significantly react with $RO_2$) in OFRs with initial NO injection (OFR-iNO) based on the argument that its lifetime is too short due to large amounts of $O_3$ OH, and $HO_2$ to compete with $RO_2$+$HO_2$ (Li et al., 2015). We evaluate this issue below by calculating NO effective lifetime ($\tau_{NO}$, in s), defined as NO exposure ($NO_{exp}$, in molecules $cm^{-3}$ s) divided by initial NO concentration, under various conditions. This definition cannot effectively capture the true NO average lifetime if it is close to or longer than the residence time. In this case, $\tau_{NO}$ close to the residence time will be obtained, which is still long enough for our characterization purposes.

#### 3.1.1 OFR185-iNO

In OFR185-iNO, NO is *not* oxidized extremely quickly under *all* conditions. For instance, under a typical condition in the midrange of the phase space shown in Fig. 1a, $\tau_{NO}$ ~13 s. This lifetime is much shorter than the residence time, but long enough for $OH_{exp}$ to reach ~$3x10^{10}$ molecules $cm^{-3}$ s, which is equivalent to an OH equivalent age of ~6 hrs. Such an OH equivalent age is already sufficient to allow some VOC processing and even SOA formation to occur (Lambe et al., 2011; Ortega et al., 2016). Within $\tau_{NO}$, NO suppresses $HO_2$ through the reaction NO+$HO_2$→$NO_2$+OH, leading to $NO_{exp}/HO_{2exp}$ of ~700 during this period, high enough for $RO_2$ to dominantly react with NO. Meanwhile, NO+$HO_2$→$NO_2$+OH enhances OH production, which helps $OH_{exp}$ build up in a relatively short period. In addition, non-tropospheric photolysis of VOCs at 185 and 254 nm is minor ($F185_{exp}/OH_{exp}$ ~ 600 cm/s, Fig. 1a), because of enhanced OH production and moderate UV. Therefore, such an OFR condition may be of some interest for high-NO VOC oxidation. We thus analyze the $NO_y$ chemistry in OFR185-iNO in more detail below, by taking the case shown in Fig. 1a as a representative example.

In OFR185-iNO, $HO_x$ concentrations are orders-of-magnitude higher than in the atmosphere while the amount of $O_3$ produced is relatively small during the first several seconds after the flow enters the reactor. As a result, NO is not oxidized almost exclusively by $O_3$ as in the troposphere, but also by OH and $HO_2$ to form HONO and $NO_2$, respectively (Fig. 1a). The large concentration of OH present then oxidizes HONO to $NO_2$, and $NO_2$ to $HNO_3$. Photolysis only plays a negligible role in the fate of HONO and $NO_2$ in OFRs, in contrast to the troposphere, where it is the main fate of these species. This is because the reactions of HONO and $NO_2$ with OH are greatly accelerated in OFR compared to those in the troposphere, while photolysis not (Peng et al., 2016). The interconversion between $NO_2$ and $HO_2NO_2$ is also greatly accelerated (Fig. 1a), since a large amount of $HO_2$ promotes the formation of $HO_2NO_2$, whose thermal decomposition and reaction with OH in turn enhance the recycling of $NO_2$. Though not explicitly modeled in this study, $RO_2$ are expected to undergo similar reactions with $NO_2$ to form reservoir species, i.e., peroxynitrates (Orlando and Tyndall, 2012). Peroxynitrates that decompose on

timescales considerably longer than OFR residence times may serve as effectively permanent $NO_y$ sinks in OFRs (see Section 3.4.1).

Interestingly but not surprisingly, the $NO_y$ chemistry shown in Fig. 1a is far from temporally uniform during the OFR residence time (Fig. S1a). Within $\tau_{NO}$, NO undergoes an e-fold decay as it is rapidly converted into $NO_2$ and HONO, whose concentrations reach maxima around that time. After most NO is consumed, HONO and $NO_2$ also start to decrease, but significantly more slowly than NO, since they do not have as many and efficient loss pathways as NO. The reaction of OH with HONO, the dominant fate of HONO, is slower than that with NO (Fig. 1a). The net rate of the $NO_2$-to-$HO_2NO_2$ conversion becomes low because of the relatively fast reverse reaction (Fig. 1a). Besides, the total loss of $NO_2$ is partially offset by the production from HONO. The generally stable concentrations of HONO and $NO_2$ (Fig. S1a) result in their respective reaction rates with OH that are comparable during and after $\tau_{NO}$ (Fig. 1a), as OH variation is also relatively small during the entire residence time (Fig. S1b). However, the $NO_2$-to-$HO_2NO_2$ conversion after $\tau_{NO}$ is much faster than during it (Fig. 1a), resulting from substantially decreased NO and $HO_2$ concomitantly increasing >1 order of magnitude after $\tau_{NO}$ (Fig. S1a,b). $HNO_3$ and $HO_2NO_2$, which are substantially produced only after $NO_2$ is built up, have much higher concentrations later than within $\tau_{NO}$.

Under other OFR185-iNO conditions than in Fig. 1a, the major reactions interconverting $NO_y$ species are generally the same, although their relative importance may vary. At lower $NO^{in}$, the perturbation of $HO_x$ chemistry caused by $NO_y$ species is smaller. Effects of $NO^{in}$ less than 1 ppb (e.g., typical non-urban ambient concentrations) are generally negligible regarding $HO_x$ chemistry. Regarding $NO_y$ species, the pathways in Fig. 1a are still important under those conditions. At higher $NO^{in}$ (e.g., >1 ppm), one might expect $NO_3$ and $N_2O_5$ to play a role (as in OFR254-iNO; see Section 3.1.2 below), since high $NO_y$ concentrations might enhance self/cross reactions of $NO_y$. However, this would not occur unless OH production is high, since relatively low $O_3$ concentrations in OFR185-iNO cannot oxidize $NO_2$ to $NO_3$ rapidly. Also, a large amount of $NO_y$ can lead to significant OH suppression. That would in turn slow down the $NO_3$ production from $HNO_3$ by OH. This is especially true when an OFR is used to oxidize the output of highly concentrated sources (e.g., from vehicle exhausts). When sources corresponding to $OHR_{ext}$ of thousands of $s^{-1}$ and $NO^{in}$ of tens of ppm are injected into OFR185 (Fig. 1b), they essentially inhibit active chemistry except NO consumption, as all subsequent products are much less abundant compared to remaining NO (Fig. S1c).

### 3.1.2 OFR254-iNO

The ppm-level $O_{3,in}$ used in the OFR254-iNO mode of operation has a strong impact on its $NO_y$ chemistry. An $O_{3,in}$ of 2.2 ppm (lowest in this study) is already enough to shorten $\tau_{NO}$ to ~1 s, preventing NO from playing a role in the chemistry under most explored conditions. The reaction fluxes under a typical $O_{3,in}$ of 7 ppm are shown in Fig. 1c. A reactive flux from $NO+O_3 \rightarrow NO_2$ makes the reaction of NO with other oxidants (OH, $HO_2$ etc.) negligible. The $HNO_3$ production pathway from $NO_2$ is similar to that in OFR185-iNO. The interconversion between $NO_2$ and $HO_2NO_2$ is also fast over the residence time, and even faster than in OFR185-iNO during $\tau_{NO}$, since a high concentration of $O_3$ also controls the OH-$HO_2$

297 interconversion and makes $HO_2$ more resilient against suppression due to high NO (Fig. S1f; Peng et al.,
298 2015). A major difference in the $NO_y$ chemistry in OFR254-iNO (Fig. 1c) compared to OFR185-iNO (Fig.
299 1a) is significant $NO_3/N_2O_5$ chemistry due to high $O_3$ in OFR254-iNO, which accelerates the oxidation of
300 $NO_2$ to $NO_3$. Interconversion between $NO_2+NO_3$ and $N_2O_5$ also occurs to a significant extent because of
301 high $NO_2$. Under the conditions of Fig. 1c, $NO_3$ can also be significantly consumed by $HO_2$. Unlike
302 OFR185-iNO, OFR254-iNO can substantially form $NO_3$ from $HNO_3$ under conditions that are not on the
303 extremes of the explored physical condition space, e.g., at higher UV and lower $NO^{in}$ (e.g., Fig. S2). In
304 the case of very high $NO^{in}$ (equal to or higher than $O_{3,in}$), all $O_3$ can be rapidly destroyed by NO. As a
305 consequence, OH production is shut down and these cases are of little practical interest (Fig. S3h).

306 **3.1.3 Uncertainty analysis**

307 The results of uncertainty propagation confirm that the output uncertainties due to uncertain
308 kinetic parameters are relatively low compared to other factors (e.g., non-plug flow in OFR; Peng et al.,
309 2015) and the overall model accuracy compared to experimental data (a factor of 2–3; Li et al., 2015).
310 For OFR185-iNO, NO, $NO_3$, and OH exposures have relative uncertainties of ~0–20%, ~40–70%, and ~15–
311 40%, respectively. The uncertainties in OH exposure are very similar to those in the cases without $NO_x$
312 (Peng et al., 2015). The contribution of $NO_y$ reactions to $OH_{exp}$ uncertainty is negligible, except for some
313 contribution of OH+NO→HONO in a few cases with high $NO^{in}$ (Fig. 2). The uncertainties on $NO_{exp}$ are
314 dominated by the reactions producing $HO_x$ and $O_3$, i.e., the major consumers of NO. For $NO_3$ exposure,
315 a few major production and loss pathways (e.g., $NO_2+NO_3→N_2O_5$, $N_2O_5→NO_2+NO_3$, and
316 $HO_2+NO_3→OH+NO_2+O_2$) dominate its uncertainties. OFR254-iNO has a simpler picture of parametric
317 uncertainties in terms of composition. $O_3$ controls the NO oxidation under most conditions and this
318 reaction contributes most of output uncertainties for NO exposures. $HO_2+NO_3→OH+NO_2+O_2$ dominates
319 the uncertainty on $NO_3$ exposure. The levels of those uncertainties are lower than in OFR185-iNO (<2%
320 for NO exposure; <60% in all cases and <25% in most cases for $NO_3$ exposure). Thus, model uncertainties
321 in OFR254-iNO are not shown in detail.

322 **3.2 Different conditions types**

323 Having illustrated the main $NO_y$ chemical pathways for typical cases, we present the results of
324 the exploration of the entire physical parameter space (see Section 2.2). Note that the explored space
325 is indeed very large and gridded logarithmically uniformly in every dimension. Therefore, the statistics
326 of the exploration results can be useful to determine the relative importance of the conditions types
327 defined in Section 2.2 and Table 3.

328 It has been shown that during $\tau_{NO}$, $RO_2$ can react dominantly with NO (Section 3.1.1), while to
329 determine if a condition is high-NO (see Table 3), the entire residence time is considered. This is done
330 because for VOC oxidation systems of interest, there will be significant oxidation of the initial VOC and
331 its products under low-NO conditions, if $\tau_{NO}$ is shorter than the reactor residence time. After most NO
332 is consumed, the longer the remaining residence time, the more $RO_2$ will react with $HO_2$ and the more
333 likely that an input condition is classified as low-NO. For a condition to be high-NO, a significantly long
334 $\tau_{NO}$ is required. Figure 3 shows the fractional occurrence distribution of good/risky/bad conditions in

the entire explored condition space over logarithm of $r(RO_2+NO)/r(RO_2+HO_2)$, which distinguishes high- and low-NO conditions. In OFR254-iNO, $\tau_{NO}$ is so short that no good high-NO condition is found in the explored range in this study (Fig. 3a). A fraction of explored conditions are bad high-NO. These conditions result from a full consumption of $O_3$ by NO. Then very little $HO_x$ is produced (right panels in Fig. S3h), but the fate of any $RO_2$ formed is dominated by $RO_2$+NO (right panels in Fig. S3i). However, also due to negligibly low OH concentration, little $RO_2$ is produced and non-tropospheric photolysis of VOCs is also substantial compared to their reaction with OH under these conditions, classifying all of them as "bad" (Fig. 3a).

In OFR185-iNO, in addition to the typical case shown in Fig. 1a, many other cases have a $\tau_{NO}$ of ~10 s or longer (Figs. S3b and S4), which allow the possibility of high-NO conditions. Indeed, ~1/3 of explored conditions in OFR185-iNO with a residence time of 3 min are high-NO (Fig. 3b). Most of these high-NO conditions are also classified as bad, similar with those in OFR254-iNO. More importantly, in contrast to OFR254-iNO, good and risky high-NO conditions also comprise an appreciable fraction of the OFR185-iNO conditions. It is easily expected that very high $OHR_{ext}$ and $NO^{in}$ lead to bad high-NO conditions (all panels in Fig. 4), since they strongly suppress $HO_x$, which yields bad conditions and in turn keep NO destruction relatively low. Besides, the occurrence of bad high-NO conditions is reduced at high UV (bottom panels in Fig. 4), which can be explained by lowered NO due to high $O_3$ production and fast OH reactant loss due to high OH production. Good high-NO conditions are rare in the explored space. They are only 1.1% of total explored conditions (Fig. 3b) and present under very specific conditions, i.e., higher $H_2O$, lower UV, lower $OHR_{ext}$, and $NO^{in}$ of tens to hundreds of ppb (Figs. 4 and S5). Since a very high NO can suppress OH, to obtain both a significant NO level and a good conditions, $NO^{in}$ can only be tens to hundreds of ppb. As $NO^{in}$ is lower and OH is higher than under bad high-NO conditions, UV should be lower than bad high-NO conditions to keep a sufficiently long presence of NO. Thus, UV at 185 nm for good high-NO conditions are generally lower than $10^{12}$ photons $cm^{-2}$ $s^{-1}$ (Fig. S5). In addition, a low $OHR_{ext}$ (generally <50 $s^{-1}$) and a higher $H_2O$ (the higher the better, although there is no apparent threshold) are also required for good high-NO conditions (Fig. S5), as Peng et al. (2016) pointed out. Risky high-NO conditions often occur between good and bad high-NO conditions, e.g., at lower $NO^{in}$ than bad conditions (e.g., Cases ML, MM, HL, and HM in Fig. 4, see Table 2 for the typical case label code), at higher $OHR_{ext}$ and/or $NO_{in}$ than good conditions (e.g., Cases ML and MM), and at lower $H_2O$ than good conditions (e.g., Case LL).

The trend of the distributions of good, risky, and bad low-NO conditions is generally in line with the analysis in Peng et al. (2016). For low-NO conditions, $NO_y$ species can be simply regarded as external OH reactants, as in Peng et al. (2016). As $H_2O$ decreases and/or $OHR_{ext}$ or $NO^{in}$ increases, a low-NO condition becomes worse (good→risky→bad) (Figs. 4 and 5). In OFR185-iNO, increasing UV generally makes a low-NO condition better because of an OH production enhancement (Fig. 4); while in OFR254-iNO, increasing UV generally makes a low-NO condition worse (Fig. 5), since at a higher UV, more $O_3$ is destroyed and the resilience of OH to suppression is reduced.

As discussed above, the fraction of high-NO conditions also depends on OFR residence time. A

shorter residence time is expected to generally lead to a larger fraction of high-NO conditions, since the time spent in the reaction for $t > \tau_{NO}$ is significantly smaller. Thus, we also investigate an OFR185-iNO case with a residence time of 30 s. In Fig. 3b, compared to the case with a residence time of 3 min, the distributions of all condition types (good/risky/bad) of the 30 s residence time case shift toward higher $r(RO_2+NO)/r(RO_2+HO_2)$. Nevertheless, shortening the residence time also removes the period when the condition is better (i.e., less non-tropospheric photolysis), when external OH reactants have been partially consumed and OH suppression due to $OHR_{ext}$ has been reduced later in the residence time. As a result, the fractions of good and risky conditions decrease (Fig. 3b). With the two effects (higher $r(RO_2+NO)/r(RO_2+HO_2)$ and more significant non-tropospheric photolysis) combined, the fraction of good high-NO conditions increases by a factor of ~3. An even shorter residence time does not result in a larger good high-NO fraction, since the effect of enhancing non-tropospheric photolysis is even more apparent.

### 3.3 Effect of non-plug flow

We performed model runs where the only change with respect to our box model introduced in Section 2.2 is that the plug-flow assumption is replaced by the residence time distribution (RTD) measured by Lambe et al. (2011) (also see Fig. S8 of Peng et al. (2015)). The chemistry of different air parcels with different residence times is simulated by our box model and outputs are averaged over the RTD. Lateral diffusion between different air parcels is neglected in these simulations.

$OH_{exp}$ calculated from the mode with RTD ($OH_{exp,RTD}$) is higher than that calculated from the plug-flow model ($OH_{exp,PF}$) in both OFR185-iNO and OFR254-iNO (Table 4 and Fig. S6). Under most explored conditions deviations are relatively small, which leads to an overall positive deviation of $OH_{exp,RTD}$ from $OH_{exp,PF}$ by ~x2 (within the uncertainties of the model and its application to real experimental systems). For OFR185-iNO, most conditions (~90%) in the explored space lead to <x3 differences between $OH_{exp,PF}$ and $OH_{exp,RTD}$, while for a small fraction of cases the differences can be larger (Fig. S6). The larger deviations are mainly present at high UV, $OHR_{ext}$, and $NO^{in}$, where conditions are generally “bad” and in which experiments are of little atmospheric relevance. Under these specific conditions, external OH reactants and $NO_y$ can be substantially destroyed for the air parcels with residence times longer than the average, while this is not the case for the average residence time. This feature was already described by Peng et al. (2015) (see Fig. S10 of that study). Although only non-$NO_y$ external OH reactants were considered in that study, the results are the same. In the present study, a higher upper limit of the explored $OHR_{ext}$ range (compared to Peng et al., 2015, due to trying to simulate extremely high $OHR_{ext}$ used in some recent literature studies) large amounts of $NO_y$ and cause somewhat larger deviations. In OFR254-iNO, OH is less suppressed at high $OHR_{ext}$ and $NO^{in}$ than in OFR185-iNO because of high $O_3$ (Peng et al., 2015), $OH_{exp,RTD}$ deviations from $OH_{exp,PF}$ are also smaller (Table 4).

Based on the outputs of the model with RTD, similar mapping of the physical input space as Figs. 4 and 5 can be done (Figs. S7 and S8). Overall, the mapping of the RTD model results is very similar with that of the plug-flow model. The conditions appear to be only slightly better in a few places of the explored space than those from the plug-flow model, which can be easily explained by the discussions

411 above. Besides, the mapping in Figs. S7 and S8 also appear to be slightly more low-NO, for the same
412 reasons discussed above. After NO is destroyed at long residence times, $HO_2$, suppressed by NO, also
413 recovers as OH. $r(RO_2+NO)/r(RO_2+HO_2)$ is obviously expected to be smaller than in the plug-flow model
414 in general.

415 Note that most conditions that appear to be better in the RTD model results are already
416 identified as bad by the plug-flow model. Those conditions look slightly better only because of their
417 better *RTD-averaged* $F185_{exp}/OH_{exp}$ and $F254_{exp}/OH_{exp}$. However, each of those cases is actually
418 composed of both a better part at longer residence times and also a worse part at shorter residence
419 times. Under those conditions, the reactor simultaneously works in two distinct regimes, one of which
420 is bad due to heavy OH suppression. Such conditions are obviously not desirable for OFR operation.

421 **3.4 Possible issues related to high-$NO_x$ levels**

422 In the discussion above, we focused on obtaining high-NO conditions and considered only one
423 experimental issue (non-tropospheric photolysis) that had been previously investigated in Peng et al.
424 (2016) and is not specific for experiments with high NO injection. We discuss additional potential
425 reasons why the OFR-iNO chemistry can deviate strongly from tropospheric conditions, as specifically
426 related to high-$NO_x$ level in this subsection.

427 **3.4.1 $NO_2$**

428 $NO_2$ reacts with $RO_2$ to form peroxynitrates, generally regarded as reservoir species in the
429 atmosphere as most of them thermally decompose very quickly compared to atmospheric time scales.
430 However, in OFRs, with residence times on the order of minutes, some peroxynitrates may no longer be
431 considered as fast decomposing. This is especially true for acylperoxy nitrates, whose lifetimes can be
432 hours at room temperature (Orlando and Tyndall, 2012). Acylperoxy nitrates are essentially sinks instead
433 of reservoirs in OFRs for both $NO_2$ and $RO_2$. $RO_2$ is estimated to be as high as several ppb in OFRs by our
434 model (e.g., ~6 ppb $RO_2$ in OFR185 at $H_2O$=1%, UV at 185 nm=$1x10^{13}$ photons $cm^{-2}$ $s^{-1}$, $OHR_{ext}$=1000 $s^{-1}$,
435 and $NO^{in}$=0), while high-NO experiments can yield far higher $NO_2$. If all $RO_2$ were acylperoxy, the $RO_2$
436 chemistry could be rapidly shut down by $NO_2$, as rate constants of these $RO_2 + NO_2$ reactions are around
437 $10^{-11}$ $cm^3$ $molecule^{-1}$ $s^{-1}$ (Orlando and Tyndall, 2012). Nevertheless, acylperoxy nitrates are not expected
438 to typically be the dominant component of peroxynitrates, since acyl radicals are not a direct oxidation
439 product of most common VOCs and can only be formed after several steps of oxidation (Atkinson and
440 Arey, 2003; Ziemann and Atkinson, 2012). Most alkylperoxy nitrates retain their short-lived reservoir
441 characteristics in OFRs due to their relatively short thermal decomposition time scales (on the order of
442 0.1 s; Orlando and Tyndall, 2012). Even so, OFR experiments can be seriously hampered at extremely
443 high $NO_2$. If $NO_2$ reaches ppm levels, the equilibrium between $RO_2+NO_2$ and alkylperoxy nitrate
444 ($RO_2+NO_2 \leftrightarrow RO_2NO_2$) is greatly shifted toward the alkylperoxy nitrate side, as the forward and reverse
445 rate constants are on the order of $10^{-12}$ $cm^3$ $molecule^{-1}$ $s^{-1}$ and 1 $s^{-1}$, respectively (Orlando and Tyndall,
446 2012). This results in a substantial decrease in effective $RO_2$ concentration, or in other words, a
447 substantial slow-down of $RO_2$ chemistry.

448 Parts per million levels of $NO_2$ may impose an additional experimental artifact in the oxidation

chemistry of aromatic precursors. OH-aromatic adducts, i.e., the immediate products of aromatic oxidation by OH, undergo addition of $O_2$ and $NO_2$ at comparable rates under ppm levels of $NO_2$ (rate constants of the additions of $O_2$ and $NO_2$ are on the order of $10^{-16}$ and $10^{-11}$ molecules $cm^{-3}$ $s^{-1}$, respectively ;Atkinson and Arey, 2003). However, only the former addition is atmospherically relevant (Calvert et al., 2002). Liu et al. (2015) performed OFR254-iNO experiments with toluene over a range of $NO^{in}$ of 2.5–10 ppm, encompassing the NO concentration range at which the reactions of OH-toluene adduct with $O_2$ and with $NO_2$ are of equal importance (~5 ppm; Atkinson and Arey, 2003). This suggests that nitroaromatics, whose formation was reported in the study of Liu et al. (2015), might have been formed in substantial amounts in that study through the addition of $NO_2$ to the OH-toluene adduct.

### 3.4.2 $NO_3$

As discussed in Section 3.1, $NO_3$ can be formed in significant amounts in OFRs with high NO injection. Although $NO_3$ is also present in the atmosphere, especially during nighttime, significant VOC oxidation by both OH and $NO_3$ results in more complex chemistry that may complicate the interpretation of experimental results. $NO_3$ oxidation-only OFR has been previously realized experimentally via thermal dissociation of injected $N_2O_5$ (Palm et al., 2017). We discuss below how to avoid significant VOC oxidation by $NO_3$ and achieve OH-dominated VOC oxidation in OFRs with high NO injection.

If $NO_{3exp}/OH_{exp} > 0.1$, $NO_3$ can be a competitive reactant for biogenic alkenes and dihydrofurans, which have a C=C bond for $NO_3$ addition, and phenols, which have activated hydroxyl for fast hydrogen abstraction by $NO_3$ (Atkinson and Arey, 2003), while for lower $NO_{3exp}/OH_{exp}$, OH is expected to dominate the oxidation of all VOCs, as shown in Fig. 6. Oxidation for VOCs without alkene C=C bonds and phenol hydroxyl (such as alkanes and (alkyl)benzenes) is dominated by OH unless $NO_{3exp}/OH_{exp} > 1000$. Despite its double bond, ethene reacts as slowly with $NO_3$ as alkanes, likely due to lack of alkyl groups enriching electron density on the C=C bond, which slows $NO_3$ addition. We calculate $NO_{3exp}/OH_{exp}$ for OFR185-iNO and OFR254-iNO and plot histograms of this ratio in Fig. 6. Many experimental conditions lead to high enough $NO_{3exp}/OH_{exp}$ that $NO_3$ is a competitive sink for alkenes, while only under very extreme conditions can $NO_3$ be a competitive sink for species without C=C bonds. High-NO conditions in OFR185-iNO have lower $NO_{3exp}/OH_{exp}$ (~$10^{-2}$–$10^{2}$) than in OFR254-iNO (~$10^{1}$–$10^{5}$) (Figs. 6 and S3d,g,j). This difference in $NO_{3exp}/OH_{exp}$ is due to the different levels of $O_3$ in the two modes, as high $O_3$ promotes $NO_2$-to-$NO_3$ oxidation. Note that low-NO conditions in both OFR185-iNO and OFR254-iNO can also reach high $NO_{3exp}/OH_{exp}$ as some high-NO conditions have. This is because in OFR185-iNO a large part of $NO_3$ is formed by OH oxidation, resulting in $NO_{3exp}/OH_{exp}$ being largely influenced by $NO^{in}$ but not by other factors mainly governing OH (Fig. S3d); and under low-NO conditions in OFR254-iNO, $NO_3$ can form rapidly from $NO_2+O_3$, while OH can be heavily suppressed by high $OHR_{ext}$ (Fig. S3g,j).

Most of the species shown in Fig. 6 are primary VOCs, except phenols and a dihydrofuran, which can be intermediates of the atmospheric oxidation of (alkyl)benzenes (Atkinson and Arey, 2003) and long-chain alkanes (Aimanant and Ziemann, 2013; Strollo and Ziemann, 2013; Ranney and Ziemann, 2016), respectively. Nevertheless, only the phenol production may occur in high-NO OFRs, as the

particle-phase reaction in the photochemical formation of dihydrofurans from alkanes is too slow compared to typical OFR residence times (Ranney and Ziemann, 2016). Therefore, the impact of $NO_3$ oxidation on VOC fate needs to be considered only if the OFR input flow contains high NO mixed with biogenics and/or aromatics [(alkyl)benzenes and/or phenols]. However, (alkyl)benzenes were likely to be major SOA precursors in, to our knowledge, the only few literature OFR studies with high NO levels (Ortega et al., 2013; Tkacik et al., 2014; Liu et al., 2015). In the study of the air in a traffic tunnel (OFR185-iNO mode; Tkacik et al., 2014), where toluene is usually a major anthropogenic SOA precursor as in other urban environments (Dzepina et al., 2009; Borbon et al., 2013; Hayes et al., 2015; Jathar et al., 2015), $NO_x$ was several hundreds of ppb. This resulted in an estimated $NO_{3exp}/OH_{exp}$ range of ~0.1–1, where up to ~30% of cresols (intermediates of toluene oxidation) may have been consumed by $NO_3$. Dihydrofurans may also have formed in the tunnel air (but outside the OFR) in the presence of $NO_x$ (Aimanant and Ziemann, 2013; Strollo and Ziemann, 2013) and, after entering the OFR, they would have been substantially (up to ~50%) consumed by $NO_3$. In the laboratory experiment of Liu et al. (2015) with toluene, the injection of as much as 10 ppm NO elevated $NO_{3exp}/OH_{exp}$ to ~100, where cresols from toluene oxidation reacted almost exclusively with $NO_3$ in addition to being photolyzed.

### 3.4.3 A case study

We use a case study of an OFR254-13-iNO laboratory experiment with a large amount of toluene (5 ppm) and $NO^{in}$ (10 ppm) to illustrate how very high VOC and NO concentrations cause multiple types of atmospherically irrelevant reactions in OFR. Due to very high $OHR_{ext}$ and $NO^{in}$, photolysis of toluene at 254 nm may have been important (Peng et al., 2016). In case of a high (close to 1) quantum yield, up to ~80% of the consumed toluene in their experiments could have been photolyzed (Scheme 1). Of the rest of reacted toluene, ~10% undergoes H-abstraction by OH from the methyl group in the model, leading to an $RO_2$ similar to alkyl $RO_2$ and likely proceeding with normal $RO_2$ chemistry. ~90% of the toluene formed an OH-adduct (Calvert et al., 2002). As discussed above, 70% of this adduct (depending on $NO^{in}$) is predicted to recombine with $NO_2$ producing nitroaromatics because of the ppm-level $NO_x$. The adduct could also react with $O_2$ via two types of pathways, of which one was addition forming a special category of $RO_2$ (OH-toluene-$O_2$ adducts) potentially undergoing ring-opening (Atkinson and Arey, 2003; Orlando and Tyndall, 2012; Ziemann and Atkinson, 2012), the other H-elimination by $O_2$ producing cresols. Again, like toluene, cresols may have been substantially photolyzed. As a result of $NO_{3exp}/OH_{exp}$ ~100, only a minor portion of cresol could have undergone OH addition and then H-elimination again. This pathway leads to the formation of methyldihydroxybenzenes and other OH-oxidation products (Atkinson and Arey, 2003). The rest of cresols may have formed methylphenoxy radicals, nevertheless, dominantly via H-abstraction by $NO_3$, since H-abstraction by OH was even a minor pathway compared to the OH-addition one (Atkinson et al., 1992). In summary, the model results suggest that there were two possible routes leading to nitroaromatic formation. However, one of them (recombination of OH-aromatic adducts with $NO_2$) is likely of little atmospheric relevance due to very high $NO_x$ needed, and the other (H-abstraction from cresol) occurs in the atmosphere but is not a major fate of aromatics (Calvert et al., 2002).

### 3.5 Implications for OFR experiments with combustion emissions as input

Emissions from combustion sources, e.g., vehicles and biomass burning, usually contain VOCs and $NO_x$ at very high concentrations (Table 1). An injection of this type of emissions (typically with $OHR_{ext}$ of thousands of $s^{-1}$ or larger and $NO^{in}$ of tens of ppm or larger) in OFRs without any pretreatment is likely to cause all experimental issues discussed in Peng et al. (2016) and this paper, i.e., strong OH suppression, substantial non-tropospheric photolysis, strong $RO_2$ suppression by $NO_2$ whether $RO_2$ is acyl $RO_2$ or not, fast reactions of $NO_2$ with OH-aromatic hydrocarbon adducts, substantial $NO_3$ contribution to VOC fate, and even a near-total inhibition of OFR chemistry due to complete titration of $O_3$ by NO in the case of OFR254. We take the study of Karjalainen et al. (2016), who used an OFR to oxidize diluted car exhaust in real-time, as an case study to investigate the extent to which these issues may affect typical combustion source studies and to explore approaches to mitigate the problems.

During the first 200 s of their experiment (defined as the "cold start" period when the catalyst is cold and emissions are high), NO and total hydrocarbon in the emissions of the test vehicle reached ~400 and ~600 ppm, respectively. We first simulate the oxidation of those emissions without any dilution (even though x12 dilution was used in their experiments) to explore the most extreme conditions. Our model simulation indicates that such an extremely concentrated source would generally lead to bad high- or low-NO conditions (depending on NO concentration) in their OFR (Fig. 7), even though it was run at relatively high $H_2O$ and UV. OH suppression can be as high as 3 orders of magnitude; VOC fates by non-tropospheric photolysis and reactions of alkenes and phenols with $NO_3$ can be nearly 100%; up to ~1/3 of OH-toluene adduct may be recombined with $NO_2$ instead of forming an adduct with $O_2$. After the test vehicle entered the "hot stabilized" stage (200–1000 s), its VOC emissions (on the order of ppm) were still too high for an undiluted OFR to yield a good condition (Fig. S9). OH suppression can still reach 2 orders of magnitude; non-tropospheric photolysis, and sometimes reactions with $NO_3$, can still dominate over reactions with OH in VOC fates; reactions of OH-toluene adduct with $NO_2$ can still be substantial at some small NO emission spikes. Moreover, although NO emissions were roughly at ppm level even during the hot stabilized period, NO effective lifetime may be very short during that period, leading to low-NO conditions in their OFR.

As suggested in Peng et al. (2016) for low-NO OFR, dilution of sources can also mitigate strong deviations on OFR-iNO chemistry vs. atmospherically-relevant conditions. A dilution by a factor of 12, as actually used by Karjalainen et al. (2016), appears to be sufficient to bring most of the hot stabilized period under good conditions (Fig. S9). However, most VOC, or in other words, most SOA formation potential, was emitted during the cold start period, when risky and bad conditions still prevailed (Figs. 7 and 8). Even if the emissions are diluted by x100, the cold-start emission peak (Fig. 7) is still under risky conditions. Although bad conditions are eliminated and good condition is present during most of time, this emission peak under risky condition may contribute >50% to total SOA formation potential (Fig. 8). For SOA formed under good condition to be dominant, a dilution factor >400 would be needed.

Note that the emissions of the test vehicle of Karjalainen et al. (2016) are rather clean compared to the typical 2013 US on-road fleet (i.e., all at the hot stabilized stage) measured by Bishop and

Stedman (2013) (Figs. 9 and S10). For emissions of an average on-road fleet, a dilution by a factor of 100 or larger would be necessary to ensure that most emissions would be processed in OFR185 under good conditions at the highest $H_2O$ and UV in this study (Figs. 9b and S10b,e,h). In the case of lower $H_2O$ and/or UV, an even larger dilution factor would be required.

Conducting OFR185-iNO experiments at high UV lowers the dilution factor needed for good conditions. However, it also renders good high-NO condition impossible (see Section 3.2 and Fig. S4). If one wants to oxidize vehicle exhausts in a high-NO environment in OFR, as in an urban atmosphere, OFR185 at low UV is necessary. Consequently, a much stronger dilution is in turn necessary to keep the operation condition still good. Nevertheless, not all vehicle emissions can be moved into good high-NO region through a simple dilution (Figs. 9c and S10c,f,i). Furthermore, a low UV would seriously limit the highest $OH_{exp}$ that OFR can achieve (~$3x10^{11}$ molecules $cm^{-3}$ s for modeled good high-NO conditions in this study), while a much higher $OH_{exp}$ would be desirable to fully convert SOA formation potential into measurable SOA mass. If both good high-NO condition and high $OH_{exp}$ are required, new techniques (e.g., injection of $N_2O$ at percent level proposed by Lambe et al. (2017)) may be necessary.

## 4 Conclusions

In this study, OFR chemistry involving $NO_y$ species was systematically investigated over a wide range of conditions. NO initially injected into the OFR was found to be rapidly oxidized under most conditions. In particular, due to high $O_3$ concentrations, NO lifetime in OFR254-iNO was too short to result in a significant $RO_2$ consumption by NO compared to that by $HO_2$ under all conditions with active chemistry. Nevertheless, it is not completely impossible for OFR185-iNO to have a significant $RO_2$ fate by NO and minor non-tropospheric photolysis at the same time ("good high-NO conditions"). According to our simulations, these conditions are most likely present at high $H_2O$, low UV, low $OHR_{ext}$, and $NO^{in}$ of tens to hundreds of ppb.

However, many past OFR studies with high NO injection were conducted under conditions remarkably different from the abovementioned very narrow range. $NO^{in}$ and/or $OHR_{ext}$ in those studies were often much higher than good high-NO conditions require (particularly, >3 orders of magnitude in some OFR studies using combustion emissions as input). In addition to non-tropospheric organic photolysis, OFR oxidation of highly concentrated sources can cause multiple large deviations from tropospheric OH oxidation, i.e., $RO_2$ suppression by high $NO_2$, substantial nitroaromatic formation from the recombination of $NO_2$ and OH-aromatic adducts, and fast reactions of VOCs with $NO_3$ compared to those with OH.

Working at lower $NO_x$ (sub-ppm level) and VOC concentrations or dilution can mitigate these experimental problems. In general, a strong dilution (by a factor of >100) is needed for OFR that process typical on-road vehicle emissions. Humidification can also make good conditions more likely. By these measures, good conditions can be guaranteed, as long as NO and/or precursor concentrations are sufficiently low, while high-NO conditions cannot be ensured. To aid design and interpretation of OFR experiments with high NO injection, we provide our detailed modeling results in a visualized form (Fig. S3). For OFR users in need for both high $OH_{exp}$ and high NO, simple NO injection is not a good option.

New techniques (e.g., injection of $N_2O$ proposed by Lambe et al. (2017) or other innovations) may be necessary to meet this need.

**Acknowledgements**

This work was partially supported by DOE (BER/ASR) DE-SC0011105 & DE-SC0016559, EPA STAR 83587701-0, and NSF AGS-1360834. We thank Pengfei Liu, Andrew Lambe, and Daniel Tkacik for providing some OFR experimental data, the authors of Karjalainen et al. (2016) and their project IEA-AMF Annex 44 for providing the data and information for the vehicle tests, Gary Bishop for providing on-road vehicle emission data, and Andrew Lambe and William Brune for useful discussions.

612 **References**


613 Aimanant, S. and Ziemann, P. J.: Chemical Mechanisms of Aging of Aerosol Formed from the Reaction
614 of n-Pentadecane with OH Radicals in the Presence of NOx, Aerosol Sci. Technol., 47(9), 979–990,
615 doi:10.1080/02786826.2013.804621, 2013.

616 Alanen, J., Simonen, P., Saarikoski, S., Timonen, H., Kangasniemi, O., Saukko, E., Hillamo, R., Lehtoranta,
617 K., Murtonen, T., Vesala, H., Keskinen, J. and Rönkkö, T.: Comparison of primary and secondary particle
618 formation from natural gas engine exhaust and of their volatility characteristics, Atmos. Chem. Phys.
619 Discuss., (February), 1–27, doi:10.5194/acp-2017-44, 2017.

620 Ammann, M., Cox, R. A., Crowley, J. N., Jenkin, M. E., Mellouki, A., Rossi, M. J., Troe, J., Wallington, T. J.,
621 Cox, B., Atkinson, R., Baulch, D. L. and Kerr, J. A.: IUPAC Task Group on Atmospheric Chemical Kinetic
622 Data Evaluation, [online] Available from: http://iupac.pole-ether.fr/#, 2016.

623 Atkinson, R. and Arey, J.: Atmospheric degradation of volatile organic compounds., Chem. Rev., 103(12),
624 4605–38, doi:10.1021/cr0206420, 2003.

625 Atkinson, R., Aschmann, S. M. and Arey, J.: Reactions of hydroxyl and nitrogen trioxide radicals with
626 phenol, cresols, and 2-nitrophenol at 296 .+-. 2 K, Environ. Sci. Technol., 26(7), 1397–1403,
627 doi:10.1021/es00031a018, 1992.

628 BIPM, IEC, IFCC, ILAC, ISO, IUPAC and IUPAPOIML: JCGM 101: 2008 Evaluation of measurement data —
629 Supplement 1 to the " Guide to the expression of uncertainty in measurement " — Propagation of
630 distributions using a Monte Carlo method., 2008.

631 Bishop, G. A. and Stedman, D. H.: Fuel Efficiency Automobile Test: Light-Duty Vehicles, [online] Available
632 from: http://www.feat.biochem.du.edu/light_duty_vehicles.html (Accessed 1 February 2017), 2013.

633 Borbon, A., Gilman, J. B., Kuster, W. C., Grand, N., Chevaillier, S., Colomb, A., Dolgorouky, C., Gros, V.,
634 Lopez, M., Sarda-Esteve, R., Holloway, J., Stutz, J., Petetin, H., McKeen, S., Beekmann, M., Warneke, C.,
635 Parrish, D. D. and De Gouw, J. A.: Emission ratios of anthropogenic volatile organic compounds in
636 northern mid-latitude megacities: Observations versus emission inventories in Los Angeles and Paris, J.
637 Geophys. Res. Atmos., 118(4), 2041–2057, doi:10.1002/jgrd.50059, 2013.

638 Burkholder, J. B., Sander, S. P., Abbatt, J., Barker, J. R., Huie, R. E., Kolb, C. E., Kurylo, M. J., Orkin, V. L.,
639 Wilmouth, D. M. and Wine, P. H.: Chemical Kinetics and Photochemical Data for Use in Atmospheric
640 Studies: Evaluation Number 18, Pasadena, CA, USA. [online] Available from:
641 http://jpldataeval.jpl.nasa.gov/, 2015.

642 Calvert, J. G., Atkinson, R., Becker, K. H., Kamens, R. M., Seinfeld, J. H., Wallington, T. H. and Yarwood,
643 G.: The Mechanisms of Atmospheric Oxidation of the Aromatic Hydrocarbons, Oxford University Press,
644 USA. [online] Available from: https://books.google.com/books?id=P0basaLrxDMC, 2002.

645 Carlton, A. G., Wiedinmyer, C. and Kroll, J. H.: A review of Secondary Organic Aerosol (SOA) formation
646 from isoprene, Atmos. Chem. Phys., 9(14), 4987–5005, doi:10.5194/acp-9-4987-2009, 2009.

647 Carter, W. P. L., Cocker, D. R., Fitz, D. R., Malkina, I. L., Bumiller, K., Sauer, C. G., Pisano, J. T., Bufalino, C.
648 and Song, C.: A new environmental chamber for evaluation of gas-phase chemical mechanisms and
649 secondary aerosol formation, Atmos. Environ., 39(40), 7768–7788,
650 doi:10.1016/j.atmosenv.2005.08.040, 2005.

651 Chameides, W., Lindsay, R., Richardson, J. and Kiang, C.: The role of biogenic hydrocarbons in urban
652 photochemical smog: Atlanta as a case study, Science (80-. )., 241(4872), 1473–1475,
653 doi:10.1126/science.3420404, 1988.

654 Cocker, D. R., Flagan, R. C. and Seinfeld, J. H.: State-of-the-Art Chamber Facility for Studying Atmospheric
655 Aerosol Chemistry, Environ. Sci. Technol., 35(12), 2594–2601, doi:10.1021/es0019169, 2001.

656 Donahue, N. M., Posner, L. N., Westervelt, D. M., Li, Z., Shrivastava, M., Presto, A. A., Sullivan, R. C.,
657 Adams, P. J., Pandis, S. N. and Robinson, A. L.: Where Did This Particle Come From? Sources of Particle
658 Number and Mass for Human Exposure Estimates, in Airborne Particulate Matter: Sources, Atmospheric
659 Processes and Health, edited by R. M. Harrison, R. E. Hester, and X. Querol, pp. 35–71, Royal Society of
660 Chemistry., 2016.

661 Dzepina, K., Volkamer, R. M., Madronich, S., Tulet, P., Ulbrich, I. M., Zhang, Q., Cappa, C. D., Ziemann, P.

J. and Jimenez, J. L.: Evaluation of recently-proposed secondary organic aerosol models for a case study in Mexico City, Atmos. Chem. Phys., 9(15), 5681–5709, doi:10.5194/acp-9-5681-2009, 2009.

George, I. J., Vlasenko, A., Slowik, J. G., Broekhuizen, K. and Abbatt, J. P. D.: Heterogeneous oxidation of saturated organic aerosols by hydroxyl radicals: uptake kinetics, condensed-phase products, and particle size change, Atmos. Chem. Phys., 7(16), 4187–4201, doi:10.5194/acp-7-4187-2007, 2007.

Haagen-Smit, A. J.: Chemistry and Physiology of Los Angeles Smog, Ind. Eng. Chem., 44(6), 1342–1346, doi:10.1021/ie50510a045, 1952.

Hallquist, M., Wenger, J. C., Baltensperger, U., Rudich, Y., Simpson, D., Claeys, M., Dommen, J., Donahue, N. M., George, C., Goldstein, A. H., Hamilton, J. F., Herrmann, H., Hoffmann, T., Iinuma, Y., Jang, M., Jenkin, M. E., Jimenez, J. L., Kiendler-Scharr, A., Maenhaut, W., McFiggans, G., Mentel, T. F., Monod, A., Prevot, A. S. H., Seinfeld, J. H., Surratt, J. D., Szmigielski, R. and Wildt, J.: The formation, properties and impact of secondary organic aerosol: current and emerging issues, Atmos. Chem. Phys., 9(14), 5155–5236, 2009.

Hayes, P. L., Carlton, a. G., Baker, K. R., Ahmadov, R., Washenfelder, R. a., Alvarez, S., Rappenglück, B., Gilman, J. B., Kuster, W. C., de Gouw, J. a., Zotter, P., Prévôt, a. S. H., Szidat, S., Kleindienst, T. E., Offenberg, J. H., Ma, P. K. and Jimenez, J. L.: Modeling the formation and aging of secondary organic aerosols in Los Angeles during CalNex 2010, Atmos. Chem. Phys., 15(10), 5773–5801, doi:10.5194/acp-15-5773-2015, 2015.

Hearn, J. D. and Smith, G. D.: Kinetics and Product Studies for Ozonolysis Reactions of Organic Particles Using Aerosol CIMS †, J. Phys. Chem. A, 108(45), 10019–10029, doi:10.1021/jp0404145, 2004.

Hoffmann, T., Odum, J. R., Bowman, F., Collins, D., Klockow, D., Flagan, R. C. and Seinfeld., J. H.: Formation of Organic Aerosols from the Oxidation of Biogenic Hydrocarbons, J. Atmos. Chem., 26(2), 189–222, doi:10.1023/A:1005734301837, 1997.

Hu, W., Palm, B. B., Day, D. A., Campuzano-Jost, P., Krechmer, J. E., Peng, Z., de Sá, S. S., Martin, S. T., Alexander, M. L., Baumann, K., Hacker, L., Kiendler-Scharr, A., Koss, A. R., de Gouw, J. A., Goldstein, A. H., Seco, R., Sjostedt, S. J., Park, J.-H., Guenther, A. B., Kim, S., Canonaco, F., Prévôt, A. S. H., Brune, W. H. and Jimenez, J. L.: Volatility and lifetime against OH heterogeneous reaction of ambient isoprene-epoxydiols-derived secondary organic aerosol (IEPOX-SOA), Atmos. Chem. Phys., 16(18), 11563–11580, doi:10.5194/acp-16-11563-2016, 2016.

Jathar, S. H., Cappa, C. D., Wexler, a. S., Seinfeld, J. H. and Kleeman, M. J.: Multi-generational oxidation model to simulate secondary organic aerosol in a 3-D air quality model, Geosci. Model Dev., 8(8), 2553–2567, doi:10.5194/gmd-8-2553-2015, 2015.

Kang, E., Root, M. J., Toohey, D. W. and Brune, W. H.: Introducing the concept of Potential Aerosol Mass (PAM), Atmos. Chem. Phys., 7(22), 5727–5744, doi:10.5194/acp-7-5727-2007, 2007.

Kang, E., Toohey, D. W. and Brune, W. H.: Dependence of SOA oxidation on organic aerosol mass concentration and OH exposure: experimental PAM chamber studies, Atmos. Chem. Phys., 11(4), 1837–1852, doi:10.5194/acp-11-1837-2011, 2011.

Karjalainen, P., Timonen, H., Saukko, E., Kuuluvainen, H., Saarikoski, S., Aakko-Saksa, P., Murtonen, T., Bloss, M., Dal Maso, M., Simonen, P., Ahlberg, E., Svenningsson, B., Brune, W. H., Hillamo, R., Keskinen, J. and Rönkkö, T.: Time-resolved characterization of primary particle emissions and secondary particle formation from a modern gasoline passenger car, Atmos. Chem. Phys., 16(13), 8559–8570, doi:10.5194/acp-16-8559-2016, 2016.

Krechmer, J. E., Pagonis, D., Ziemann, P. J. and Jimenez, J. L.: Quantification of Gas-Wall Partitioning in Teflon Environmental Chambers Using Rapid Bursts of Low-Volatility Oxidized Species Generated in Situ, Environ. Sci. Technol., 50(11), 5757–5765, doi:10.1021/acs.est.6b00606, 2016.

Lakey, P. S. J., George, I. J., Whalley, L. K., Baeza-Romero, M. T. and Heard, D. E.: Measurements of the HO2 Uptake Coefficients onto Single Component Organic Aerosols, Environ. Sci. Technol., 49(8), 4878–4885, doi:10.1021/acs.est.5b00948, 2015.

Lambe, A., Massoli, P., Zhang, X., Canagaratna, M., Nowak, J., Daube, C., Yan, C., Nie, W., Onasch, T., Jayne, J., Kolb, C., Davidovits, P., Worsnop, D. and Brune, W.: Controlled nitric oxide production via O(<sup>1</sup>D) + N<sub>2</sub>O

reactions for use in oxidation flow reactor studies, Atmos. Meas. Tech., 10(6), 2283–2298, doi:10.5194/amt-10-2283-2017, 2017.

Lambe, A. T., Ahern, A. T., Williams, L. R., Slowik, J. G., Wong, J. P. S., Abbatt, J. P. D., Brune, W. H., Ng, N. L., Wright, J. P., Croasdale, D. R., Worsnop, D. R., Davidovits, P. and Onasch, T. B.: Characterization of aerosol photooxidation flow reactors: heterogeneous oxidation, secondary organic aerosol formation and cloud condensation nuclei activity measurements, Atmos. Meas. Tech., 4(3), 445–461, doi:10.5194/amt-4-445-2011, 2011.

Lambe, A. T. and Jimenez, J. L.: PAM Wiki: Publications Using the PAM Oxidation Flow Reactor, [online] Available from: https://sites.google.com/site/pamwiki/publications (Accessed 10 February 2017), 2017.

Levy II, H.: Normal atmosphere: large radical and formaldehyde concentrations predicted., Science, 173(3992), 141–143, doi:10.1126/science.173.3992.141, 1971.

Li, R., Palm, B. B., Borbon, A., Graus, M., Warneke, C., Ortega, a M., Day, D. a, Brune, W. H., Jimenez, J. L. and de Gouw, J. a: Laboratory Studies on Secondary Organic Aerosol Formation from Crude Oil Vapors, Environ. Sci. Technol., 47(21), 12566–12574, doi:10.1021/es402265y, 2013.

Li, R., Palm, B. B., Ortega, A. M., Hu, W., Peng, Z., Day, D. A., Knote, C., Brune, W. H., de Gouw, J. and Jimenez, J. L.: Modeling the radical chemistry in an Oxidation Flow Reactor (OFR): radical formation and recycling, sensitivities, and OH exposure estimation equation, J. Phys. Chem. A, 119(19), 4418–4432, doi:10.1021/jp509534k, 2015.

Link, M. F., Friedman, B., Fulgham, R., Brophy, P., Galang, A., Jathar, S. H., Veres, P., Roberts, J. M. and Farmer, D. K.: Photochemical processing of diesel fuel emissions as a large secondary source of isocyanic acid (HNCO), Geophys. Res. Lett., 43(8), 4033–4041, doi:10.1002/2016GL068207, 2016.

Lippmann, M.: Health effects of tropospheric ozone, Environ. Sci. Technol., 25(12), 1954–1962, doi:10.1021/es00024a001, 1991.

Liu, P. F., Abdelmalki, N., Hung, H.-M., Wang, Y., Brune, W. H. and Martin, S. T.: Ultraviolet and visible complex refractive indices of secondary organic material produced by photooxidation of the aromatic compounds toluene and m-Xylene, Atmos. Chem. Phys., 15(3), 1435–1446, doi:10.5194/acp-15-1435-2015, 2015.

Mao, J., Ren, X., Brune, W. H., Olson, J. R., Crawford, J. H., Fried, a., Huey, L. G., Cohen, R. C., Heikes, B., Singh, H. B., Blake, D. R., Sachse, G. W., Diskin, G. S., Hall, S. R. and Shetter, R. E.: Airborne measurement of OH reactivity during INTEX-B, Atmos. Chem. Phys., 9(1), 163–173, doi:10.5194/acp-9-163-2009, 2009.

Martinsson, J., Eriksson, A. C., Nielsen, I. E., Malmborg, V. B., Ahlberg, E., Andersen, C., Lindgren, R., Nyström, R., Nordin, E. Z., Brune, W. H., Svenningsson, B., Swietlicki, E., Boman, C. and Pagels, J. H.: Impacts of Combustion Conditions and Photochemical Processing on the Light Absorption of Biomass Combustion Aerosol, Environ. Sci. Technol., 49(24), 14663–14671, doi:10.1021/acs.est.5b03205, 2015.

Matsunaga, A. and Ziemann, P. J.: Gas-Wall Partitioning of Organic Compounds in a Teflon Film Chamber and Potential Effects on Reaction Product and Aerosol Yield Measurements, Aerosol Sci. Technol., 44(10), 881–892, doi:10.1080/02786826.2010.501044, 2010.

Moise, T. and Rudich, Y.: Reactive Uptake of Ozone by Aerosol-Associated Unsaturated Fatty Acids: Kinetics, Mechanism, and Products, J. Phys. Chem. A, 106(27), 6469–6476, doi:10.1021/jp025597e, 2002.

Moise, T., Talukdar, R. K., Frost, G. J., Fox, R. W. and Rudich, Y.: Reactive uptake of NO3 by liquid and frozen organics, J. Geophys. Res., 107(D2), 4014, doi:10.1029/2001JD000334, 2002.

Nehr, S., Bohn, B., Fuchs, H., Häseler, R., Hofzumahaus, A., Li, X., Rohrer, F., Tillmann, R. and Wahner, A.: Atmospheric photochemistry of aromatic hydrocarbons: OH budgets during SAPHIR chamber experiments, Atmos. Chem. Phys., 14(13), 6941–6952, doi:10.5194/acp-14-6941-2014, 2014.

Nel, A.: Air Pollution-Related Illness: Effects of Particles, Science (80-. )., 308(5723), 804–806, doi:10.1126/science.1108752, 2005.

Ng, N. L., Canagaratna, M. R., Zhang, Q., Jimenez, J. L., Tian, J., Ulbrich, I. M., Kroll, J. H., Docherty, K. S., Chhabra, P. S., Bahreini, R., Murphy, S. M., Seinfeld, J. H., Hildebrandt, L., Donahue, N. M., DeCarlo, P. F., Lanz, V. a., Prévôt, a. S. H., Dinar, E., Rudich, Y., Worsnop, D. R., Prevot, A. S. H., Dinar, E., Rudich, Y. and

763 Worsnop, D. R.: Organic aerosol components observed in Northern Hemispheric datasets from Aerosol
764 Mass Spectrometry, Atmos. Chem. Phys., 10(10), 4625–4641, doi:10.5194/acp-10-4625-2010, 2010.

765 Odum, J. R., Hoffmann, T., Bowman, F., Collins, D., Flagan Richard, C. and Seinfeld John, H.: Gas particle
766 partitioning and secondary organic aerosol yields, Environ. Sci. Technol., 30(8), 2580–2585,
767 doi:10.1021/es950943+, 1996.

768 Orlando, J. J. and Tyndall, G. S.: Laboratory studies of organic peroxy radical chemistry: an overview with
769 emphasis on recent issues of atmospheric significance, Chem. Soc. Rev., 41(19), 6294,
770 doi:10.1039/c2cs35166h, 2012.

771 Ortega, A. M., Day, D. A., Cubison, M. J., Brune, W. H., Bon, D., de Gouw, J. A. and Jimenez, J. L.:
772 Secondary organic aerosol formation and primary organic aerosol oxidation from biomass-burning
773 smoke in a flow reactor during FLAME-3, Atmos. Chem. Phys., 13(22), 11551–11571, doi:10.5194/acp-
774 13-11551-2013, 2013.

775 Ortega, A. M., Hayes, P. L., Peng, Z., Palm, B. B., Hu, W., Day, D. A., Li, R., Cubison, M. J., Brune, W. H.,
776 Graus, M., Warneke, C., Gilman, J. B., Kuster, W. C., de Gouw, J., Gutiérrez-Montes, C. and Jimenez, J. L.:
777 Real-time measurements of secondary organic aerosol formation and aging from ambient air in an
778 oxidation flow reactor in the Los Angeles area, Atmos. Chem. Phys., 16(11), 7411–7433,
779 doi:10.5194/acp-16-7411-2016, 2016.

780 Palm, B. B., Campuzano-Jost, P., Day, D. A., Ortega, A. M., Fry, J. L., Brown, S. S., Zarzana, K. J., Dube, W.,
781 Wagner, N. L., Draper, D. C., Kaser, L., Jud, W., Karl, T., Hansel, A., Gutiérrez-Montes, C. and Jimenez, J.
782 L.: Secondary organic aerosol formation from in situ OH, O3, and NO3 oxidation of ambient forest air in
783 an oxidation flow reactor, Atmos. Chem. Phys., 17(8), 5331–5354, doi:10.5194/acp-17-5331-2017, 2017.

784 Palm, B. B., Campuzano-Jost, P., Ortega, A. M., Day, D. A., Kaser, L., Jud, W., Karl, T., Hansel, A., Hunter, J.
785 F., Cross, E. S., Kroll, J. H., Peng, Z., Brune, W. H. and Jimenez, J. L.: In situ secondary organic aerosol
786 formation from ambient pine forest air using an oxidation flow reactor, Atmos. Chem. Phys., 16(5),
787 2943–2970, doi:10.5194/acp-16-2943-2016, 2016.

788 Peng, Z., Carrasco, N. and Pernot, P.: Modeling of synchrotron-based laboratory simulations of Titan's
789 ionospheric photochemistry, GeoResJ, 1–2, 33–53, doi:10.1016/j.grj.2014.03.002, 2014.

790 Peng, Z., Day, D. A., Ortega, A. M., Palm, B. B., Hu, W., Stark, H., Li, R., Tsigaridis, K., Brune, W. H. and
791 Jimenez, J. L.: Non-OH chemistry in oxidation flow reactors for the study of atmospheric chemistry
792 systematically examined by modeling, Atmos. Chem. Phys., 16(7), 4283–4305, doi:10.5194/acp-16-
793 4283-2016, 2016.

794 Peng, Z., Day, D. A., Stark, H., Li, R., Lee-Taylor, J., Palm, B. B., Brune, W. H. and Jimenez, J. L.: HOx radical
795 chemistry in oxidation flow reactors with low-pressure mercury lamps systematically examined by
796 modeling, Atmos. Meas. Tech., 8(11), 4863–4890, doi:10.5194/amt-8-4863-2015, 2015.

797 Ranney, A. P. and Ziemann, P. J.: Kinetics of Acid-Catalyzed Dehydration of Cyclic Hemiacetals in Organic
798 Aerosol Particles in Equilibrium with Nitric Acid Vapor, J. Phys. Chem. A, 120(16), 2561–2568,
799 doi:10.1021/acs.jpca.6b01402, 2016.

800 Richards-Henderson, N. K., Goldstein, A. H. and Wilson, K. R.: Large Enhancement in the Heterogeneous
801 Oxidation Rate of Organic Aerosols by Hydroxyl Radicals in the Presence of Nitric Oxide, J. Phys. Chem.
802 Lett., 6, 4451–4455, doi:10.1021/acs.jpclett.5b02121, 2015.

803 Saltelli, A., Ratto, M., Tarantola, S. and Campolongo, F.: Sensitivity Analysis for Chemical Models, Chem.
804 Rev., 105(7), 2811–2828, doi:10.1021/cr040659d, 2005.

805 Sander, S. P., Friedl, R. R., Barker, J. R., Golden, D. M., Kurylo, M. J., Wine, P. H., Abbatt, J. P. D., Burkholder,
806 J. B., Kolb, C. E., Moortgat, G. K., Huie, R. E. and Orkin, V. L.: Chemical Kinetics and Photochemical Data
807 for Use in Atmospheric Studies Evaluation Number 17, Pasadena, CA, USA. [online] Available from:
808 http://jpldataeval.jpl.nasa.gov/pdf/JPL 10-6 Final 15June2011.pdf, 2011.

809 Schill, G. P., Jathar, S. H., Kodros, J. K., Levin, E. J. T., Galang, A. M., Friedman, B., Link, M. F., Farmer, D.
810 K., Pierce, J. R., Kreidenweis, S. M. and DeMott, P. J.: Ice-nucleating particle emissions from
811 photochemically aged diesel and biodiesel exhaust, Geophys. Res. Lett., 43(10), 5524–5531,
812 doi:10.1002/2016GL069529, 2016.

813 Schwantes, R. H., Schilling, K. A., McVay, R. C., Lignell, H., Coggon, M. M., Zhang, X., Wennberg, P. O. and

814 Seinfeld, J. H.: Formation of highly oxygenated low-volatility products from cresol oxidation, Atmos.
815 Chem. Phys., 17(5), 3453–3474, doi:10.5194/acp-17-3453-2017, 2017.

816 Seakins, P. W.: A brief review of the use of environmental chambers for gas phase studies of kinetics,
817 chemical mechanisms and characterisation of field instruments, EPJ Web Conf., 9, 143–163,
818 doi:10.1051/epjconf/201009012, 2010.

819 Simonen, P., Saukko, E., Karjalainen, P., Timonen, H., Bloss, M., Aakko-Saksa, P., Rönkkö, T., Keskinen, J.
820 and Dal Maso, M.: A new oxidation flow reactor for measuring secondary aerosol formation of rapidly
821 changing emission sources, Atmos. Meas. Tech., 10(4), 1519–1537, doi:10.5194/amt-10-1519-2017,
822 2017.

823 Stocker, T. F., Qin, D., Plattner, G.-K., Tignor, M., Allen, S. K., Boschung, J., Nauels, A., Xia, Y., Bex, V. and
824 Midgley, P. M.: Climate Change 2013 - The Physical Science Basis, edited by Intergovernmental Panel on
825 Climate Change, Cambridge University Press, Cambridge., 2014.

826 Strollo, C. M. and Ziemann, P. J.: Products and mechanism of secondary organic aerosol formation from
827 the reaction of 3-methylfuran with OH radicals in the presence of NOx, Atmos. Environ., 77, 534–543,
828 doi:10.1016/j.atmosenv.2013.05.033, 2013.

829 Tkacik, D. S., Lambe, A. T., Jathar, S., Li, X., Presto, A. A., Zhao, Y., Blake, D., Meinardi, S., Jayne, J. T.,
830 Croteau, P. L. and Robinson, A. L.: Secondary Organic Aerosol Formation from in-Use Motor Vehicle
831 Emissions Using a Potential Aerosol Mass Reactor, Environ. Sci. Technol., 48(19), 11235–11242,
832 doi:10.1021/es502239v, 2014.

833 Volkamer, R., Jimenez, J. L., San Martini, F., Dzepina, K., Zhang, Q., Salcedo, D., Molina, L. T., Worsnop,
834 D. R. and Molina, M. J.: Secondary organic aerosol formation from anthropogenic air pollution: Rapid
835 and higher than expected, Geophys. Res. Lett., 33(17), L17811, doi:10.1029/2006GL026899, 2006.

836 Wang, J., Doussin, J. F., Perrier, S., Perraudin, E., Katrib, Y., Pangui, E. and Picquet-Varrault, B.: Design of
837 a new multi-phase experimental simulation chamber for atmospheric photosmog, aerosol and cloud
838 chemistry research, Atmos. Meas. Tech., 4(11), 2465–2494, doi:10.5194/amt-4-2465-2011, 2011.

839 Zhang, X., Cappa, C. D., Jathar, S. H., McVay, R. C., Ensberg, J. J., Kleeman, M. J. and Seinfeld, J. H.:
840 Influence of vapor wall loss in laboratory chambers on yields of secondary organic aerosol., Proc. Natl.
841 Acad. Sci. U. S. A., 111(16), 5802–7, doi:10.1073/pnas.1404727111, 2014.

842 Ziemann, P. J. and Atkinson, R.: Kinetics, products, and mechanisms of secondary organic aerosol
843 formation, Chem. Soc. Rev., 41(19), 6582, doi:10.1039/c2cs35122f, 2012.

844

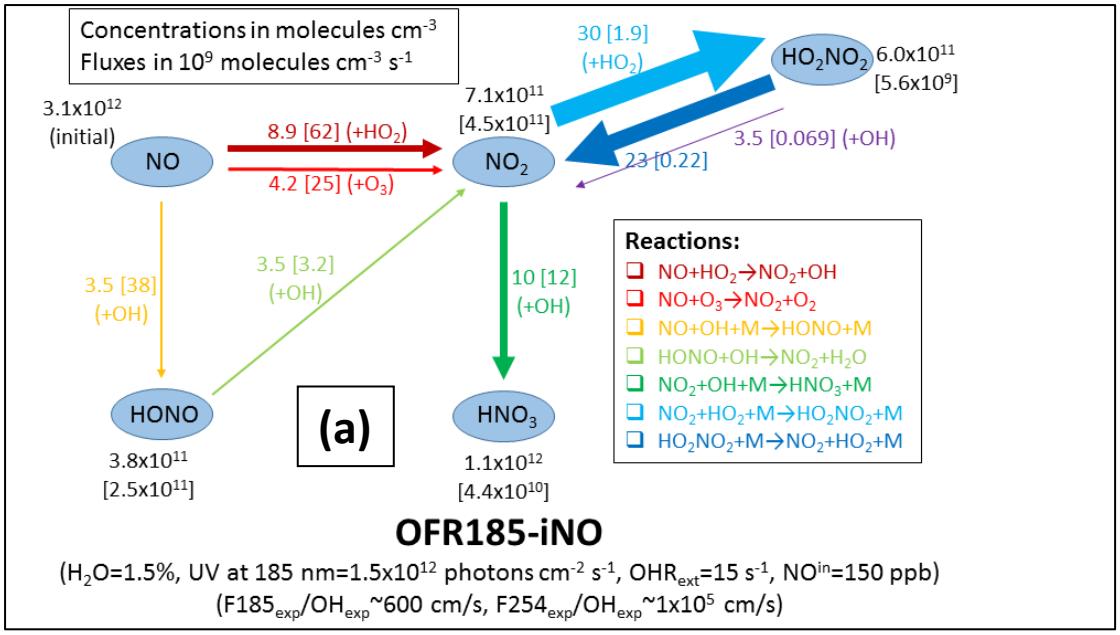


**OFR185-iNO**

($H_2O$=1.5%, UV at 185 nm=1.5x10$^{12}$ photons cm$^{-2}$ s$^{-1}$, $OHR_{ext}$=15 s$^{-1}$, $NO^{in}$=150 ppb)
($F185_{exp}/OH_{exp}$~600 cm/s, $F254_{exp}/OH_{exp}$~1x10$^5$ cm/s)

845

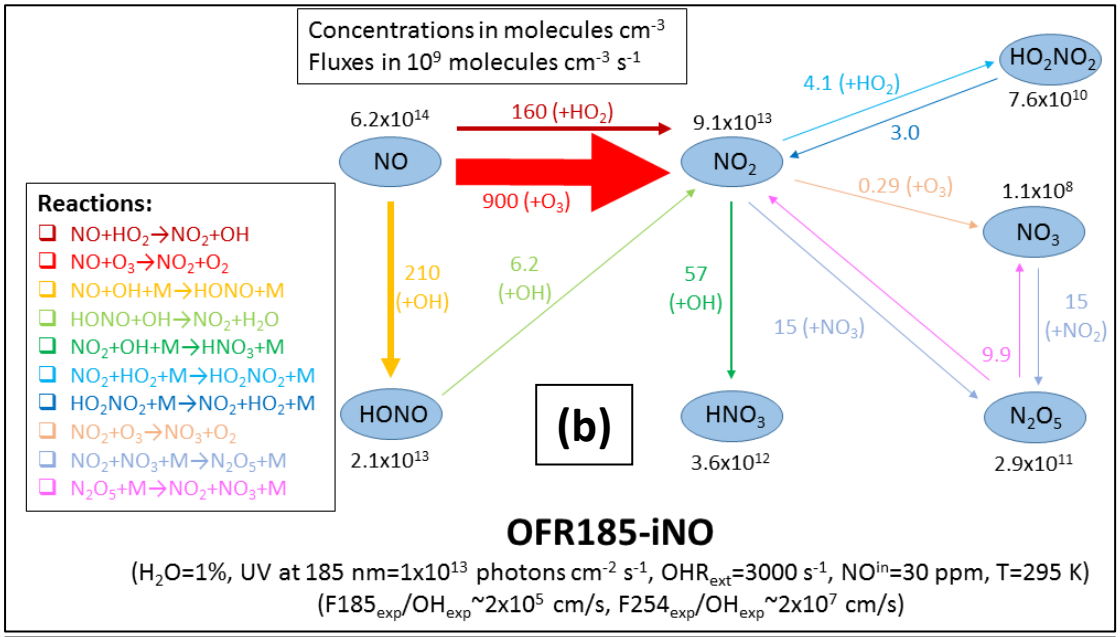


**OFR185-iNO**

($H_2O$=1%, UV at 185 nm=1x10$^{13}$ photons cm$^{-2}$ s$^{-1}$, $OHR_{ext}$=3000 s$^{-1}$, $NO^{in}$=30 ppm, T=295 K)
($F185_{exp}/OH_{exp}$~2x10$^5$ cm/s, $F254_{exp}/OH_{exp}$~2x10$^7$ cm/s)

846

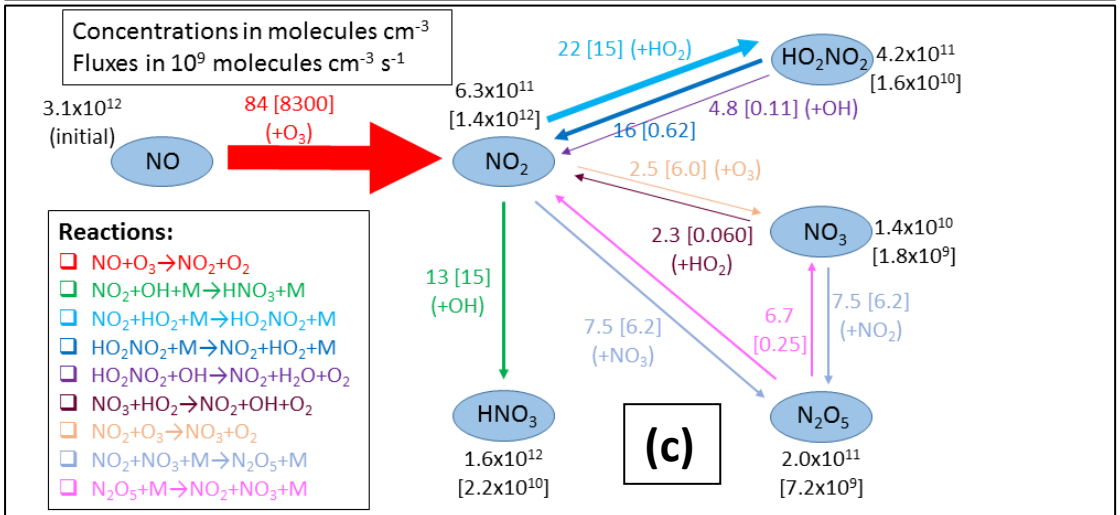


**OFR254-7-iNO**

($H_2O$=1.5%, UV at 254 nm=3.4x10$^{14}$ photons cm$^{-2}$ s$^{-1}$, $OHR_{ext}$=15 s$^{-1}$, $NO^{in}$=150 ppb, T=295 K)

847

**Figure 1.** Schematics of main N-containing species and their major interconversion pathways under typical input conditions for (a) OFR185-iNO with $NO^{in}$=150 ppb, (b) OFR254-7-iNO with $NO^{in}$=150 ppb, and (c) OFR185-iNO with $NO^{in}$=30 ppm. Species average concentrations (in molecules $cm^{-3}$) are shown in black beside species names. Arrows denote directions of the conversions. Average reaction fluxes (in units of $10^9$ molecules $cm^{-3}$ $s^{-1}$) are calculated according to the production rate, and shown on or beside the corresponding arrows and in the same color. Within each schematic, the thickness of the arrows is a measure of their corresponding species flux. Multiple arrows in the same color and pointing to the same species should be counted only once for reaction flux on a species. Note that all values in these schematics are average ones over the residence time, except for those in square brackets in panels a and b, which are average values within approximate NO effective lifetime ($\tau_{NO}$, or more accurately, an integer multiple of the model's output time step closest to NO effective lifetime). All concentrations and fluxes have two significant digits.

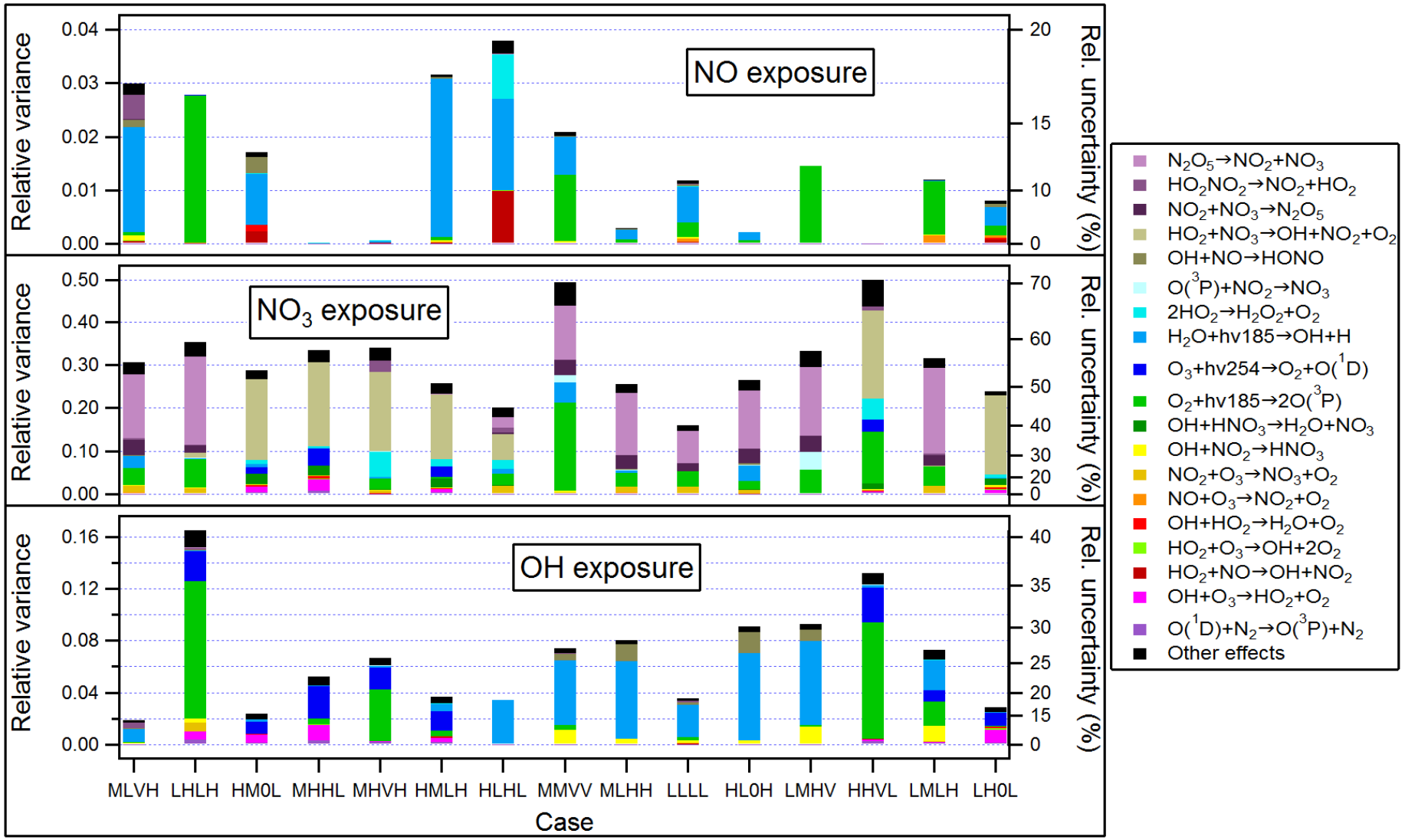
NO exposure
NO3 exposure
OH exposure
Relative variance
Rel. uncertainty (%)
Case
MLVH
LHLH
HM0L
MHHL
MHVH
HMLH
HLHL
MMVV
MLHH
LLLL
HL0H
LMHV
HHVL
LMLH
LH0L
N2O5→NO2+NO3
HO2NO2→NO2+HO2
NO2+NO3→N2O5
HO2+NO3→OH+NO2+O2
OH+NO→HONO
O(3P)+NO2→NO3
2HO2→H2O2+O2
H2O+hv185→OH+H
O3+hv254→O2+O(1D)
O2+hv185→2O(3P)
OH+HNO3→H2O+NO3
OH+NO2→HNO3
NO2+O3→NO3+O2
NO+O3→NO2+O2
OH+HO2→H2O+O2
HO2+O3→OH+2O2
HO2+NO→OH+NO2
OH+O3→HO2+O2
O(1D)+N2→O(3P)+N2
Other effects

860

**Figure 2.** Relative variances (left axes)/uncertainties (right axes) of several outputs (i.e., NO, $NO_3$, and OH exposures) of Monte Carlo uncertainty propagation, and relative contributions of key reactions to these relative variances in several typical cases (denoted in 4-character labels, see Table 2 for the typical case label code) in OFR185-iNO. Relative variances are shown in linear scales (left axis), while corresponding relative uncertainties, equal to relative variances' square roots, are indicated by the non-linear right axis. Only the reactions with a contribution of no less than 0.04 to at least one relative variance are shown.

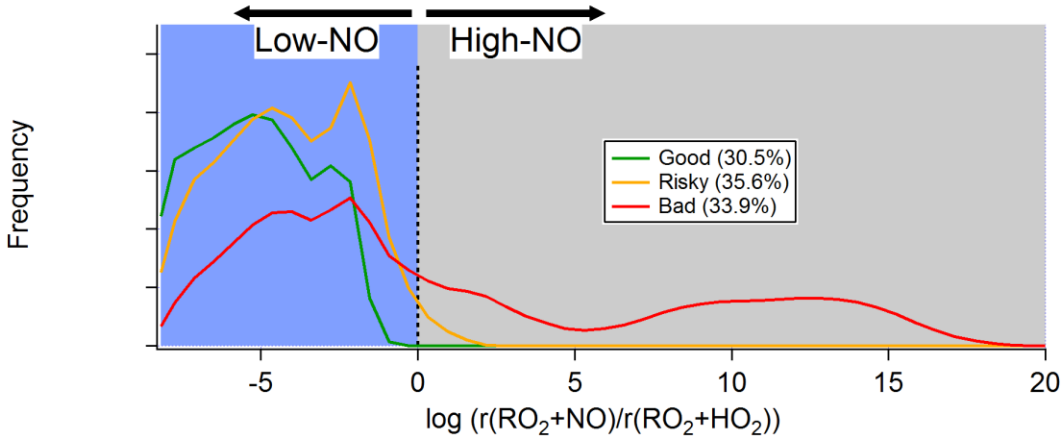


865

866 **(a) OFR254-iNO**

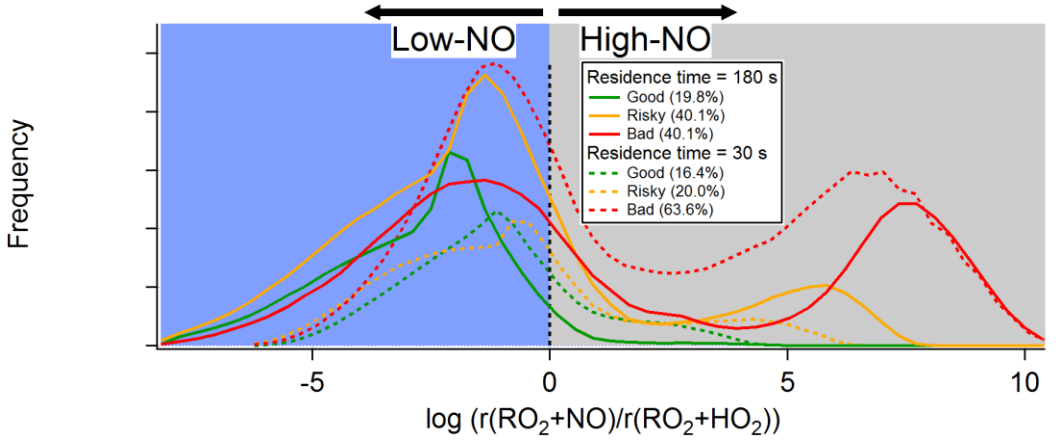


867

868 **(b) OFR185-iNO**

869 **Figure 3.** Frequency occurrence distributions of good, risky, and bad conditions (see Table 3) over
870 logarithm of the ratio between $RO_2$ reacted with NO and with $HO_2$ (see Section S1 for more detail) for
871 (a) OFR254-iNO (only the case with a residence time of 180 s) and (b) OFR185-iNO (including two cases
872 with residence times of 180 and 30 s). Low and high-NO regions (see Table 3) are colored in light blue
873 and grey, respectively.

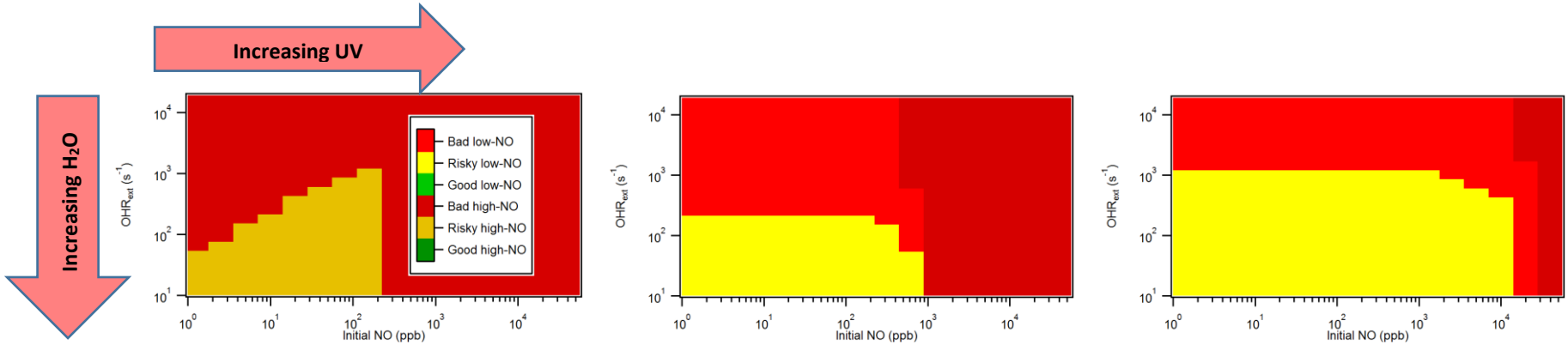
Increasing UV
Increasing H2O
Bad low-NO
Risky low-NO
Good low-NO
Bad high-NO
Risky high-NO
Good high-NO
OHRext (s-1)
Initial NO (ppb)
Case LL
Case LM
Case LH
Case ML
Case MM
Case MH
Case HL
Case HM
Case HH

882 **Figure 4.** Image plots of the condition types defined in Table 3 vs. external OH reactivity (excluding N-containing species) and initial NO for several typical cases in OFR185-
883 iNO (see Table 2 for the case label code).
884

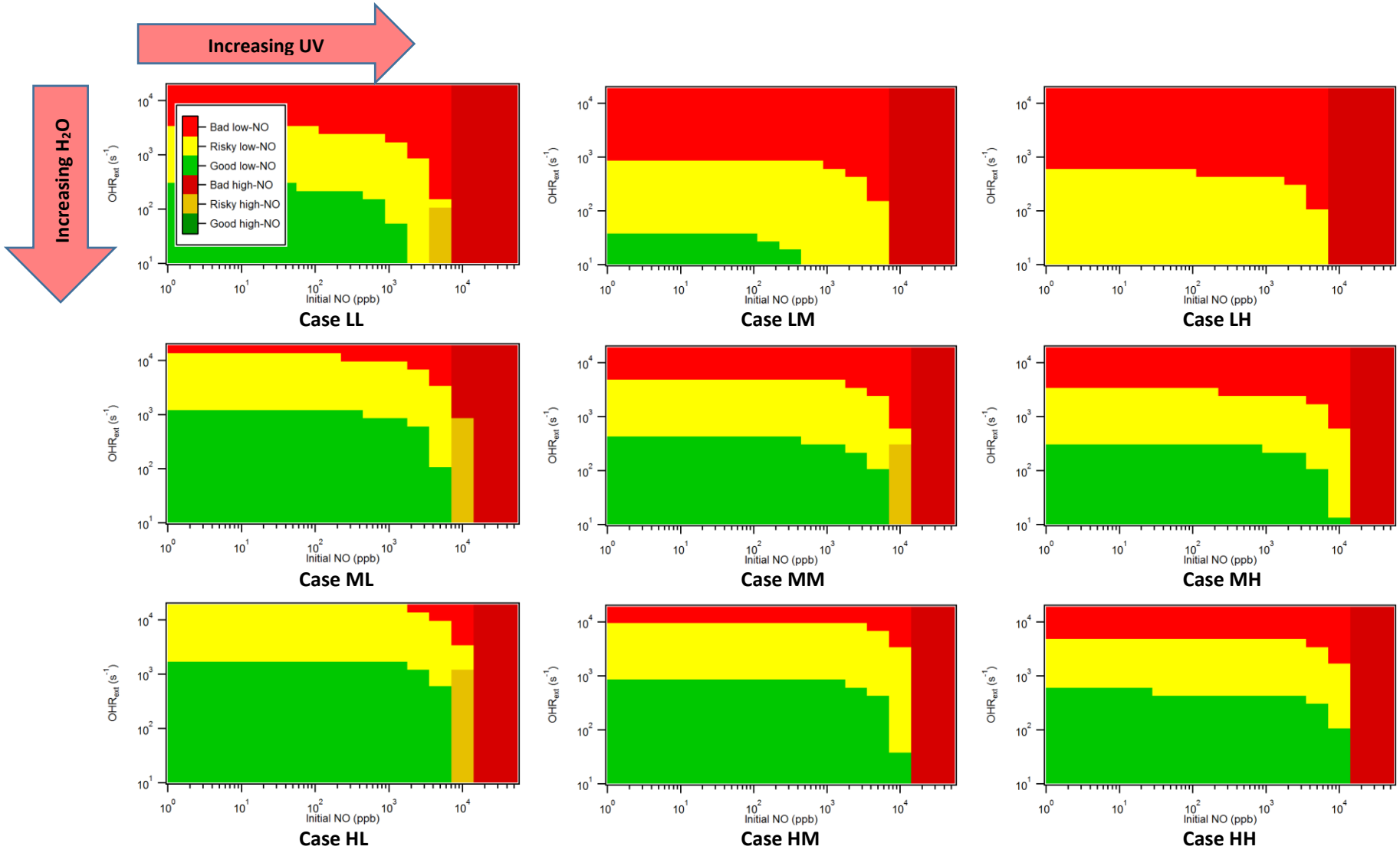
Increasing UV
Increasing H2O
Bad low-NO
Risky low-NO
Good low-NO
Bad high-NO
Risky high-NO
Good high-NO
OHRext (s-1)
Initial NO (ppb)
Case LL
Case LM
Case LH
Case ML
Case MM
Case MH
Case HL
Case HM
Case HH

893 **Figure 5.** Same format as Fig. 4, but for OFR254-22-iNO.

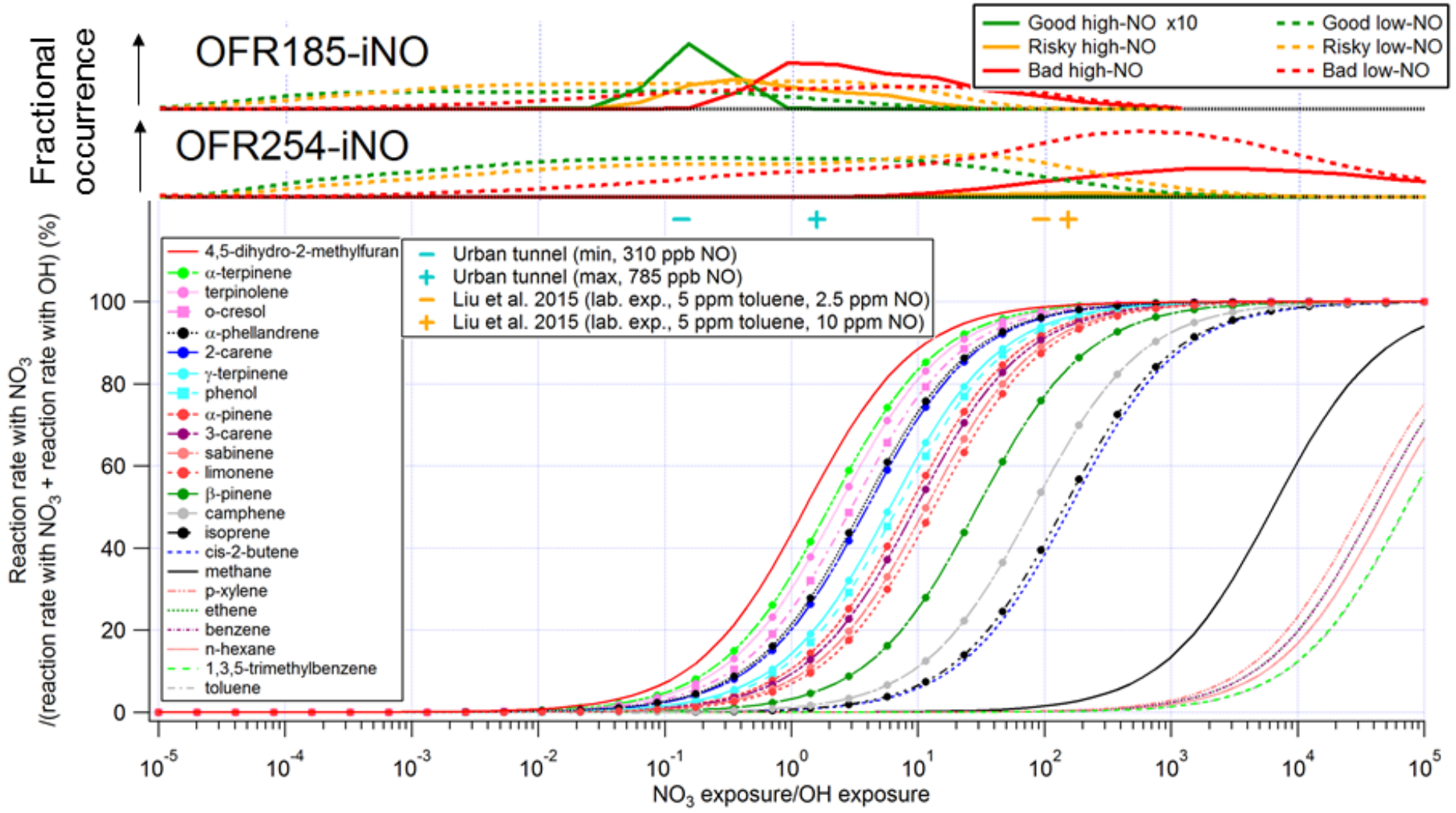


**Figure 6.** Fractional importance of the reaction rate of several species of interest with $NO_3$ vs. that with OH, as a function of the ratio of exposure to $NO_3$ and OH. The curves of biogenics and phenols are highlighted by solid dots and squares, respectively. The turquoise and orange markers show the ranges of modeled exposure ratios between $NO_3$

and OH of a source study in an urban tunnel (Tkacik et al., 2014) and a laboratory study (Liu et al., 2015) using OFR, respectively. In the upper part of the figure, the modeled frequency distributions of ratios of $NO_3$ exposure to OH exposure under good/risky/bad high/low-NO conditions for OFR185-iNO and OFR254-iNO are also shown. See Table 3 for the definitions of the three types of conditions. All curves, markers, and histograms in this figure share the same abscissa.

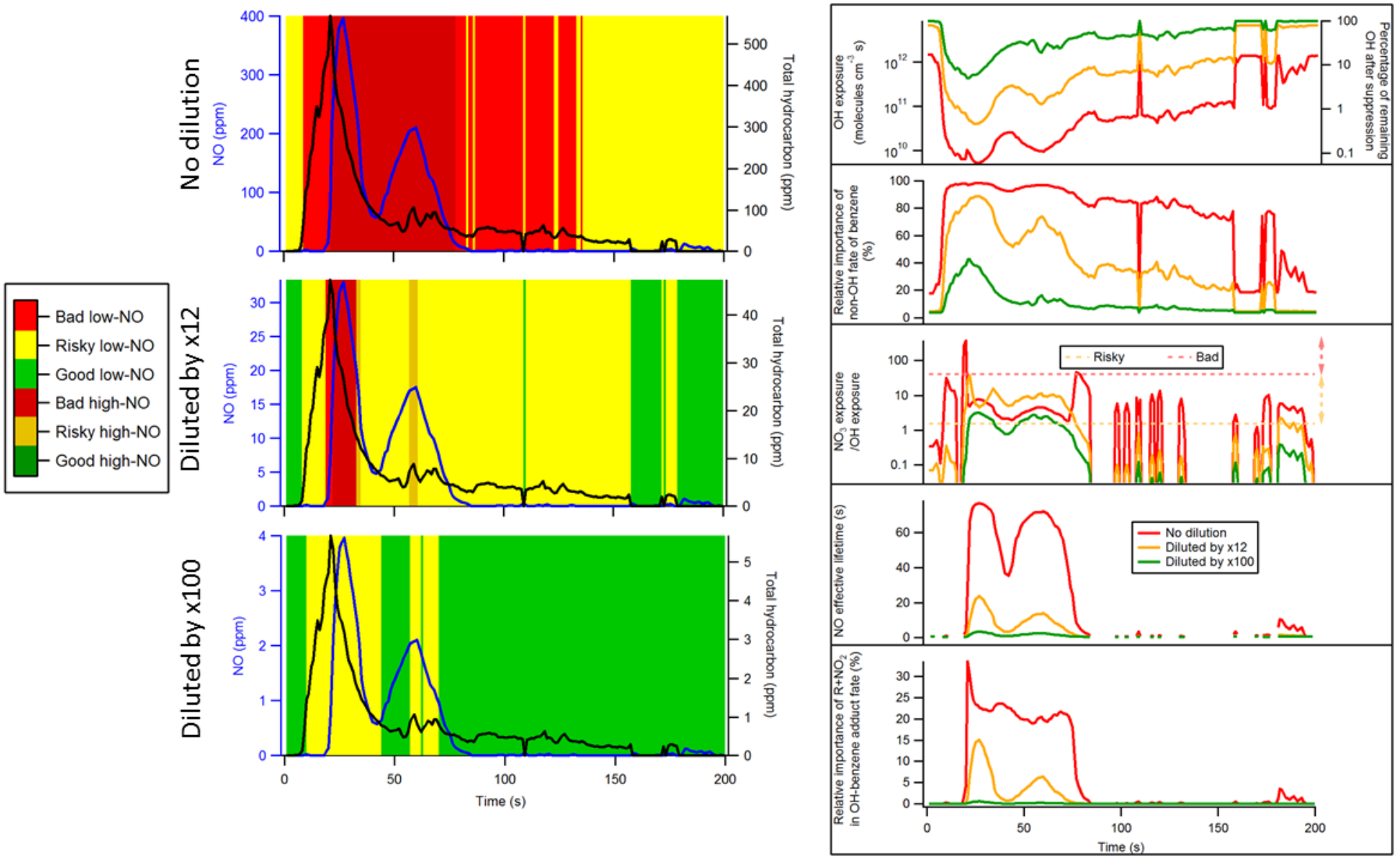
Bad low-NO
Risky low-NO
Good low-NO
Bad high-NO
Risky high-NO
Good high-NO
No dilution
Diluted by x12
Diluted by x100
NO (ppm)
Total hydrocarbon (ppm)
Time (s)
OH exposure (molecules cm$^{-3}$ s)
Percentage of remaining OH after suppression
Relative importance of non-OH fate of benzene (%)
$NO_3$ exposure /OH exposure
Risky
Bad
NO effective lifetime (s)
No dilution
Diluted by x12
Diluted by x100
Relative importance of R+$NO_2$ in OH-benzene adduct fate (%)
Time (s)

901

902 **Figure 7.** (left) NO and total hydrocarbon during the first 200 s of the test of Karjalainen et al. (2016) in the cases of no dilution, dilution by a factor of 12 (as actually done in
903 that study), and dilution by a factor of 100. Different periods of time are colored according to corresponding emissions (i.e., input conditions for OFR), classified as
904 good/risky/bad high/low-NO. (right) OH exposure/percentage of remaining OH after suppression, relative importance of non-OH fate of benzene, exposure ratio of $NO_3$ to
905 OH, NO effective lifetime, and relative importance of reaction of OH-toluene adduct with $NO_2$ in the fate of this adduct in the OFR of Karjalainen et al. (2016) during the first
906 200 s of their test in the cases of no dilution, dilution by a factor of 12, and dilution by a factor of 100. Horizontal orange and red dashed lines in the middle right panel denote
907 "risky" and "bad" regions for exposure ratio of $NO_3$ to OH, respectively. Above the orange (red) dashed line, reaction with $NO_3$ contributes >20% to the fate of phenol (isoprene).

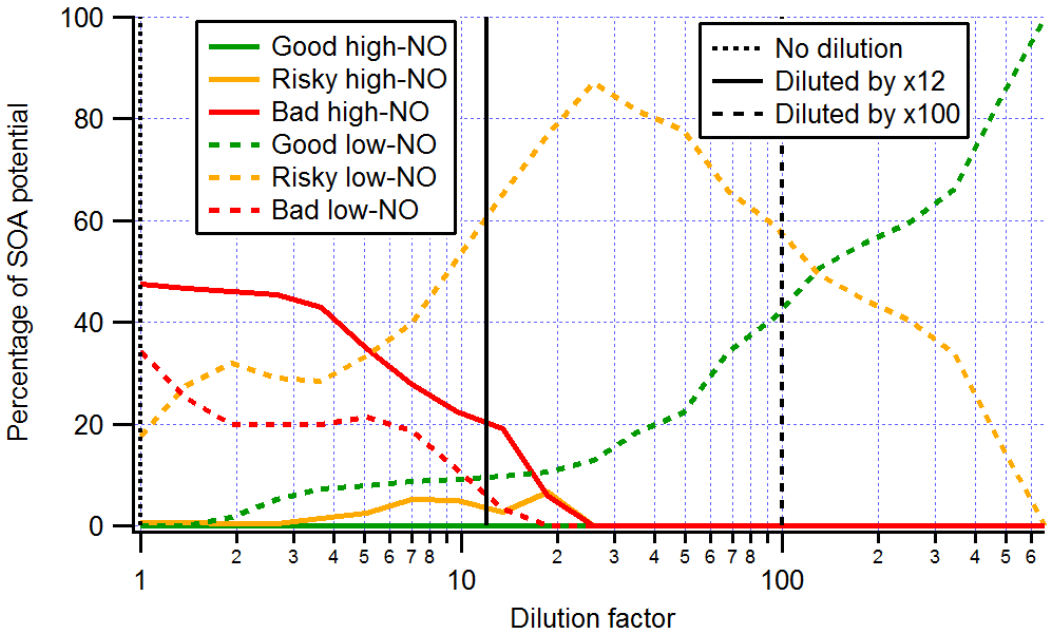


**Figure 8.** Secondary organic aerosol (SOA) potential (estimated from the total hydrocarbon measurement) in the OFR of Karjalainen et al. (2016) formed during periods of time in the OFR corresponding to good/risky/bad high/low-NO conditions, as a function of dilution factor. Vertical lines denoting dilution factors of 1, 12 (as actually used in that study), and 100 are also shown.

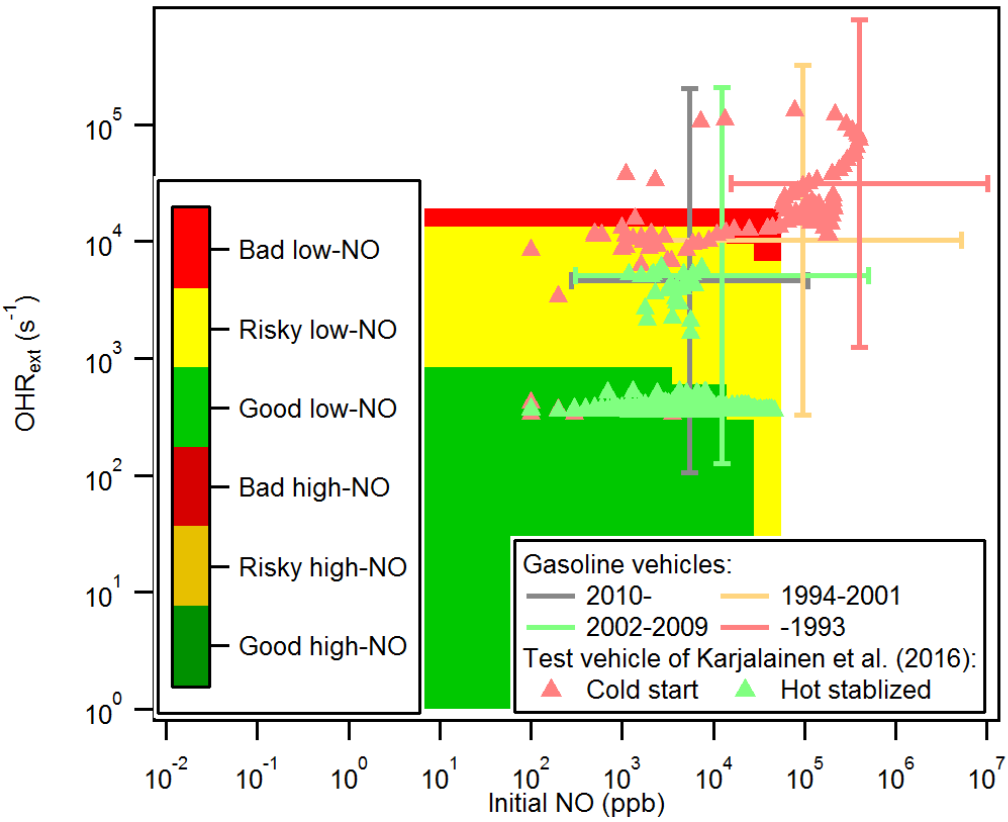


914

915 **(a) No dilution (background: Case HH)**

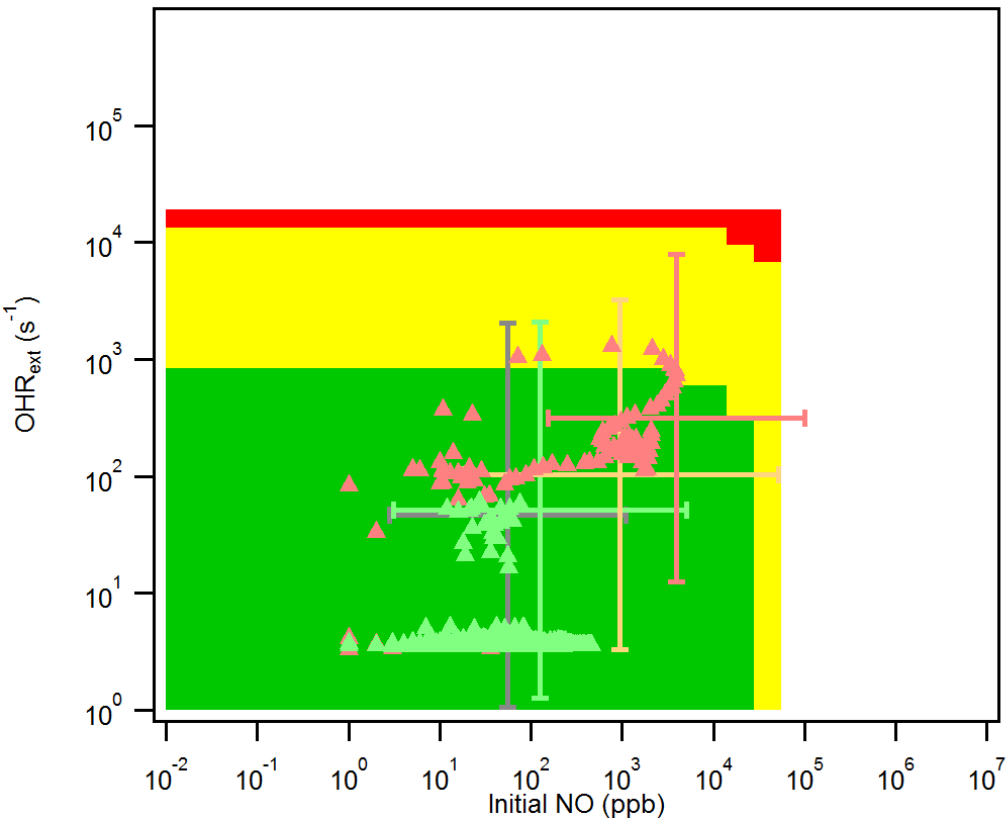


916

917 **(b) Dilution by a factor of 100 (background: Case HH)**

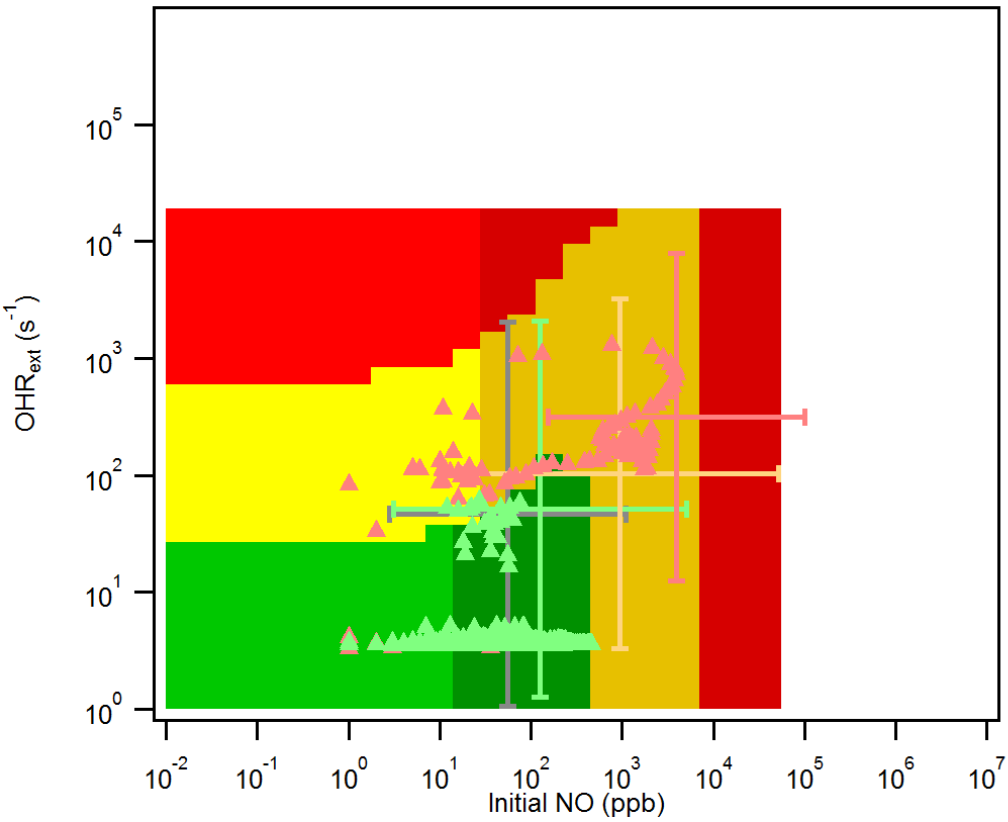


**(c) Dilution by a factor of 100 (background: Case HL)**

**Figure 9.** Location of individual 1 s datapoints vs. OFR185-iNO reaction conditions. Datapoints are shown from the test vehicle of Karjalainen et al. (2016), as well as average exhaust from gasoline vehicle on-road emissions measured by Bishop and Stedman (2013). On-road emissions are classified by vehicle year and the distribution of each category is shown as a cross representing 1 standard deviation (with log-normal distribution assumed). The X and Y axes are NO and external OH reactivity (excluding N-containing species) due to vehicle emissions in OFR in the cases of (a) no dilution and (b,c) dilution by a factor of 100. The Karjalainen et al. (2016) points are classified as cold start (during first 200 s) and hot stabilized (during 200–1000 s). In addition, the same image plots as the panels of Cases HH (high $H_2O$ and high UV, see Table 2 for the case label code) and HL in Fig. 4 (OFR185-iNO) are shown as background for comparison.

**Scheme 1.** Possible major reactions in an OFR254-13-iNO with 5 ppm toluene and 10 ppm initial NO. Branching ratios in red are estimated by the model and/or according to Calvert et al. (2002), Atkinson and Arey (2003), Ziemann and Atkinson (2012), and Peng et al. (2016). Note that addition/substitution on the aromatic ring may occur at other positions. Intermediates/products shown here are the isomers that are most likely to form. Branching ratios shown in red are not overall but from immediate reactant.

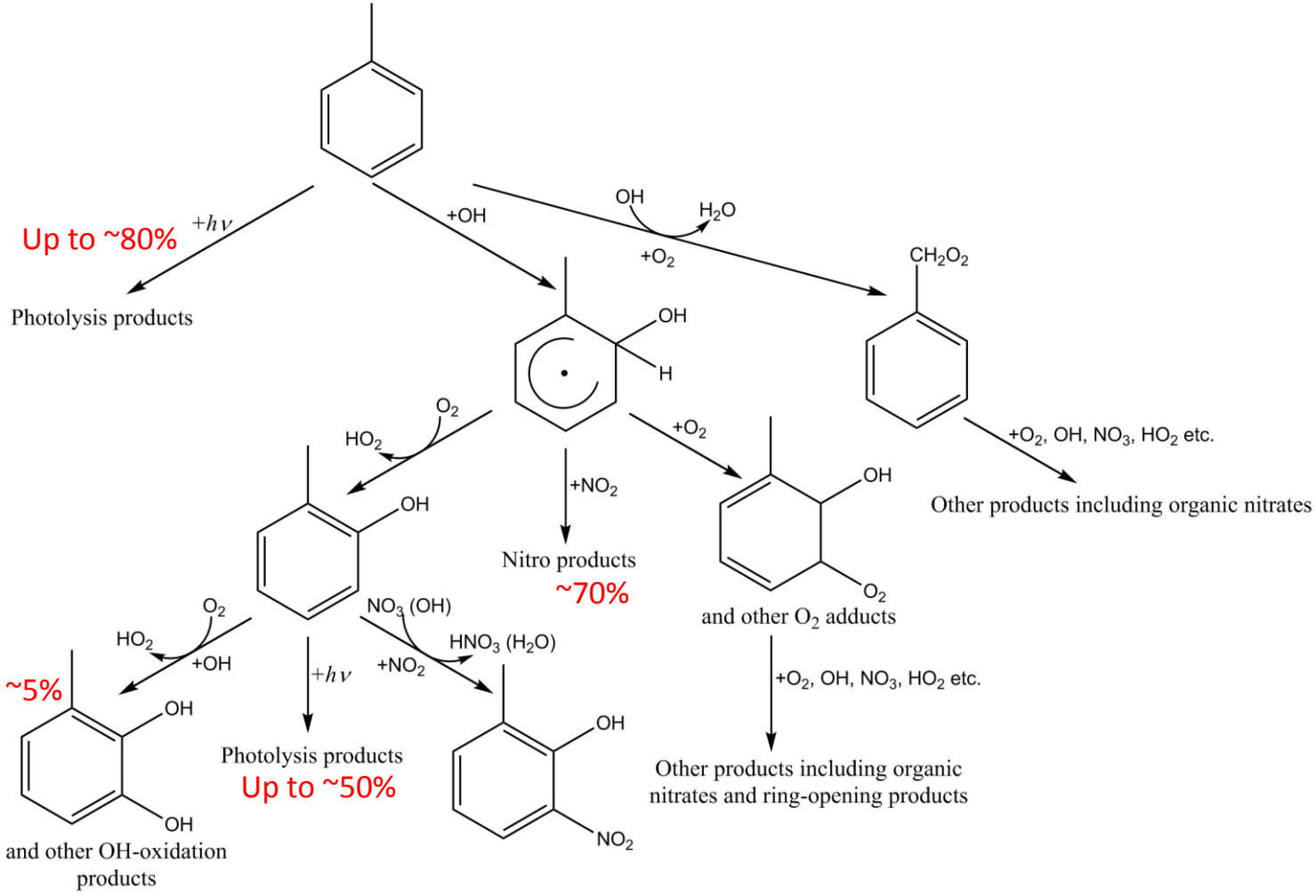

**Table 1.** Experimental conditions of several OFR studies with high NO injection.

| Study | Source type | Temperature (K) | Relative humidity (%) | Dilution factor | External OH reactivity of undiluted source ($s^{-1}$) | Source $NO_x$ concentration (ppm) |
|---|---|---|---|---|---|---|
| Link et al. (2016) | Diesel vehicle emission | | 50 | 45–110 | ~5000[*1] | 436[*1] |
| Martinsson et al. (2015) | Biomass burning emission | | | 1700 | 156400[*1] | 154 |
| Karjalainen et al. (2016) | Gasoline vehicle emission | 295 | 60 | 12 | ~73000[*2,a] | ~400[*1,b] |
| Liu et al. (2015) | Purified gas | 293 | 13 | 1 | ~1400[*1,a] | 10[*1,b] |
| Tkacik et al. (2014) | Tunnel air | 293 | 42 | 1 | ~60[*1,a] | ~0.8[*1] |
| Ortega et al. (2013) | Biomass burning emission | 290 | 30 | ~500 | ~15-500 | ~0.2 |

[*1] maximum value in the study
[*2] value at the moment of maximum NO emission
[*a] $NO_y$ species excluded
[*b] NO only

**Table 2.** Code of the labels of typical cases. A case label can be composed of four characters denoting the water mixing ratio, the photon flux, the external OH reactivity excluding N-containing species, and the initial NO mixing ratio, respectively. A case label can also be composed of two characters denoting the water mixing ratio and the photon flux.

| | | Water mixing ratio | Photon flux | External OH reactivity (no ON) | Initial NO mixing ratio |
|---|---|---|---|---|---|
| Options | | L=low (0.07%) | L=low ($10^{11}$ photons $cm^{-2}$ $s^{-1}$ at 185 nm; $4.2x10^{13}$ photons $cm^{-2}$ $s^{-1}$ at 254 nm) | 0 | 0 |
| | | M=medium (1%) | M=medium ($10^{13}$ photons $cm^{-2}$ $s^{-1}$ at 185 nm; $1.4x10^{15}$ photons $cm^{-2}$ $s^{-1}$ at 254 nm) | L=low (10 $s^{-1}$) | L=low (10 ppb) |
| | | H=high (2.3%) | H=high ($10^{14}$ photons $cm^{-2}$ $s^{-1}$ at 185 nm; $8.5x10^{15}$ photons $cm^{-2}$ $s^{-1}$ at 254 nm) | H=high (100 $s^{-1}$) | H=high (316 ppb) |
| | | | | V=very high (1000 $s^{-1}$) | V=very high (10 ppm) |
| Example | LH0V: | low water mixing ratio, high photon flux, no external OH reactivity (excluding ON), very high initial NO mixing ratio | | | |
| | ML: | medium water mixing ratio, low photon flux | | | |

**Table 3.** Definition of condition types in this study (good/risky/bad high/low-NO).

| Condition | Good | Risky | Bad |
|---|---|---|---|
| Criterion | $F185_{exp}/OH_{exp}<3x10^3$ cm $s^{-1}$ and $F254_{exp}/OH_{exp}<4x10^5$ cm $s^{-1}$ | $F185_{exp}/OH_{exp}<1x10^5$ cm $s^{-1}$ and $F254_{exp}/OH_{exp}<1x10^7$ cm $s^{-1}$ (excluding good conditions) | $F185_{exp}/OH_{exp}\geq1x10^5$ cm $s^{-1}$ or $F254_{exp}/OH_{exp}\geq1x10^7$ cm $s^{-1}$ |
| Condition | High-NO | | Low-NO |
| Criterion* | $\frac{r(RO_2+NO)}{r(RO_2+HO_2)} > 1$ | | $\frac{r(RO_2+NO)}{r(RO_2+HO_2)} \leq 1$ |

* See Section S1 for detail.

949 **Table 4.** Statistics of the ratio between OH exposures calculated in the model with the Lambe et al. (2011) residence time distribution ($OH_{exp,RTD}$) and in the plug-flow model
950 ($OH_{exp,PF}$). The geometric mean, uncertainty factor (geometric standard deviation), and percentage of outlier cases (>3 or <1/3) are shown for OFR185-iNO, OFR254-70-iNO,
951 and OFR254-7-iNO.

| | Geometric mean | Uncertainty factor | Outlier cases (%) |
|---|---|---|---|
| OFR185-iNO | 1.91 | 1.64 | 11 |
| OFR254-7-iNO | 1.59 | 1.51 | 7 |
| OFR254-70-iNO | 1.48 | 1.29 | 3 |

952